REVIEW

Check for updates

Current state of copper-based bimetallic materials for electrochemical CO$_2$ reduction: a review

Otmane Zoubir, [iD] [a] Lahoucine Atourki, [iD] *[a] Hassan Ait Ahsaine [iD] *[b] and Amal BaQais[c]

The increasing CO$_2$ concentration in the atmosphere has caused profound environmental issues such as global warming. The use of CO$_2$ as a feedstock to replace traditional fossil sources holds great promise to reduce CO$_2$ emissions. The electrochemical conversion of CO$_2$ has attracted much attention because it can be powered by renewable sources such as solar energy. In this review article, we provide insight into the important parameters when studying CO$_2$RR and give a comprehensive review on the description of synthesis methods with electrocatalytic CO$_2$ reduction over bimetallic copper-based materials. Due to the important bibliographic data on Cu bimetallic materials, we have limited this review to Sn, In, Pd, Zn and Ag. At the end of this review, challenges and perspectives for further upgrading have been included to briefly highlight the important future considerations of this rapidly growing technology.

1. Introduction

The intensification of human industrial activities has gradually disrupted environmental stability on earth, causing more CO$_2$ production.[1] The increasing CO$_2$ concentration level in the atmosphere has resulted in severe problems such as the greenhouse effect, leading to global warming, melting glaciers, and more disastrous weather.[2] Therefore, it is of critical importance to reduce atmospheric CO$_2$ concentration. To this end, much effort has been devoted to define potential methods to mitigate CO$_2$ emissions. An appealing solution is to use CO$_2$ as the carbon source to produce value-added products such as carbon monoxide (CO), formic acid (HCOOH), formate (HCOO$^-$), methanol (CH$_3$OH), methane (CH$_4$), ethylene (C$_2$H$_4$), ethanol (C$_2$H$_5$OH), as well as others by applying the renewable energy as energy input.[3] A variety of alternative CO$_2$ utilization approaches are being studied, including biological,[4] thermochemical,[5,6] photochemical[7–10] and electrochemical methods.[11–14] For thermochemical CO$_2$ conversion *via* a reforming process, it requires not only high reaction temperatures and pressures but also an equal amount of hydrogen as the reducing agent, which is energetically hazardous for large-scale applications. For the photochemical process, the selectivity and production rate of the photocatalytic active systems are too low to be economically valid. In contrast,

CO$_2$ electrochemical reduction (CO$_2$RR) appears to be one of the most promising technologies owing to its feasible operating conditions, scalability, and the increasing sources of green electricity with zero-CO$_2$ emissions.[15] However, challenges still exist such as slow electron transfer kinetics resulting in low exchange current densities, low energetic efficiency, and poor selectivity.[16]

The development of efficient electrocatalysts plays a key role in the electrochemical reduction of CO$_2$ in terms of activity and selectivity.[17] Over the last few decades, enormous efforts have been devoted into investigating CO$_2$ electrocatalysts for the electrochemical CO$_2$ reduction reaction (CO$_2$RR).[2] The most commonly explored electrocatalysts for CO$_2$ reduction can be divided into three groups: metallic; non-metallic; molecular catalysts. Polycrystalline monometallic catalysts offer unique merits such as simple structure, ease of handling, robustness, and other advantages, making them particularly appealing candidates for fundamental research.[14] Based on the primary CO$_2$ reduction product, four distinct groups of monometallic catalysts have been identified: (1) CO selective metals such as (Pd, Au, Zn, Ag, and Ga); (2) metals that mainly produce HCOOH (*e.g.*, Hg, Pb, Cd, In, Sn, and Ti); (3) metals that form hydrocarbons such as CH$_4$ and C$_2$H$_4$ (*e.g.*, Cu); (4) metals that mainly produce hydrogen, H$_2$ (Ni, Pt, Fe, and Ti). Among all the aforementioned monometallic CO$_2$ electrocatalysts, copper (Cu) is the only metal that can deeply reduce CO$_2$ to products such as hydrocarbons and alcohols with acceptable activity and efficiency.[18] However, the selectivity of Cu toward certain products is typically poor.[19] Recently, there has been growing interest in bimetallic catalysts for CO$_2$ reduction; they represent new trends and opportunities in electrochemical CO$_2$

[a]MANAPSE Lab, Faculty of Sciences, Mohammed V University in Rabat, Morocco. E-mail: l.atourki@um5r.ac.ma

[b]Laboratoire de Chimie Appliquée des Matériaux, Faculty of Sciences, Mohammed V University in Rabat, Morocco. E-mail: h.aitahsaine@um5r.ac.ma

[c]Department of Chemistry, College of Science, Princess Nourah bint Abdulrahman University, P.O. Box 84428, Riyadh 11671, Saudi Arabia

conversion.[20,21] Metals and metal oxide-based catalysts especially the Cu based electrocatalysts have been substantially reported as efficient CO_2RR catalysts.[22–24]

They are easy to synthesize, relatively stable in working conditions. These materials do not require special preparation conditions compared to other molecular. Many remarkable contributions that have been reported using serious preparation control of structures in morphological tailoring,[25] steering surfaces,[23] Metal atom decoration,[26] atomic scale structuration,[27] guided alloying,[28,29] electrolyte design,[30] and strained surfaces.[31] As robust as Cu based electrodes are, they still suffer from a reconstruction during electrolysis. This double-edged sword can degrade the efficiency of the catalysts with altering the well-defined Cu morphology and highly active sites,[32,33] or reconstructs the generating unique Cu active sites with increased catalytic activity for specific products.[34]

The focus throughout this article will be on the use of copper-based bimetallic materials to reduce carbon dioxide into value-Added products. We have reviewed the Cu-M electrocatalysts (M: Sn, In, Pd, Zn and Ag) as they the most important reported electrocatalysts for CO_2RR in the last decade. In this article, we will start by discussing the basic principles of CO_2 electroreduction, including thermodynamics, reaction mechanism, and factors influencing CO_2 electroreduction. Next, we will look at the electrochemical methods for CO_2 electroreduction. Finally, copper-based bimetallic materials will be discussed in detail, including synthesis approaches and catalytic performance.

2. Fundamentals of electrocatalytic CO_2 reduction

2.1 Thermodynamics of CO_2 reduction

In thermodynamic, the Gibbs free energy (G) can be used to determine the maximum amount of reversible work that can be derived from any system at constant pressure (P) and temperature (T). The change in Gibbs energy ΔG can be used to measure the spontaneity of a specific reaction. If the Gibbs free energy decreases while the reaction proceeds, the reactants will spontaneously be converted into products. If G increases, the reaction will spontaneously proceed in the opposite direction, thereby making the starting materials.[35]

In electrochemistry, Gibbs energy can be accurately controlled by applied potential as shown in equation (Qiao *et al.* 2016):[36]

$$\Delta G = -nFE_{cell} \tag{1}$$

where n represents the number of electrons transferred during the electrochemical process, E_{cell} is the cell potential, and F is Faraday's constant.

This equation indicates the quantitative relationship between chemical energy and electrical energy in cell reactions (Table 1).

2.2 Reaction mechanism

Researchers across the world have devoted tremendous effort to understand the mechanism for CO_2 electrochemical reduction.

Table 1 Standard Gibbs energies of formation at 298 K, 1 atm (ref. 37)

Product	Gibbs free energy ΔG (kJ mol^{-1})
C	0
CO	−137.3
CO_2	−394.4
CH_4	−50.8
C_2H_4	−68.1
CH_3OH	−161.6
H_2O (steam)	−228.6
H_2O (water)	−237.2
O_2	0
H_2	0

Especially, why different metals generate different products. In this regard, they have proposed many pathways for electrochemical reduction (ERC), and continue to propose novel reaction pathways based on their understanding of CO_2 reduction on metallic electrodes. However, since ERC is a surface phenomenon, there is no generalized reaction towards the products obtained. The mechanism must depend on the type and morphology of the catalyst.[38,39] The electrochemical reduction of CO_2 is a multi-step reaction process that may proceed *via* two to fourteen electron reaction pathways (Table 2) and yielding diverse reduction products. This multi-step reaction generally involves three major steps: (1) chemical adsorption of CO_2 on the surface of the catalyst; (2) electron/proton transfer to separate C–O bonds and/or form C–H bonds; (3) desorption of products from the surface of electrocatalyst and diffusion into the electrolyte.[40]

In a typical CO_2 electrolyzer, anode and cathode are placed into two chambers separated with an ion-conducting membrane. At the anode, water is oxidized to form molecular oxygen, while CO_2 is reduced to form carbon species at the cathode. The thermodynamic potential that allows the one-electron reduction of CO_2 to form CO_2^- is −1.90 V *vs.* SHE in pH 7.0 aqueous solution, making the reaction uphill and unfavorable.[41–43] The first step involves one-electron transfer to generate a key intermediate CO_2^-, which is the rate-limiting step in the reaction. In contrast, proton-assisted multi-electron transfer processes are more advantageous and take place almost

Table 2 Standard electrochemical potentials for CO_2 reduction[16,54]

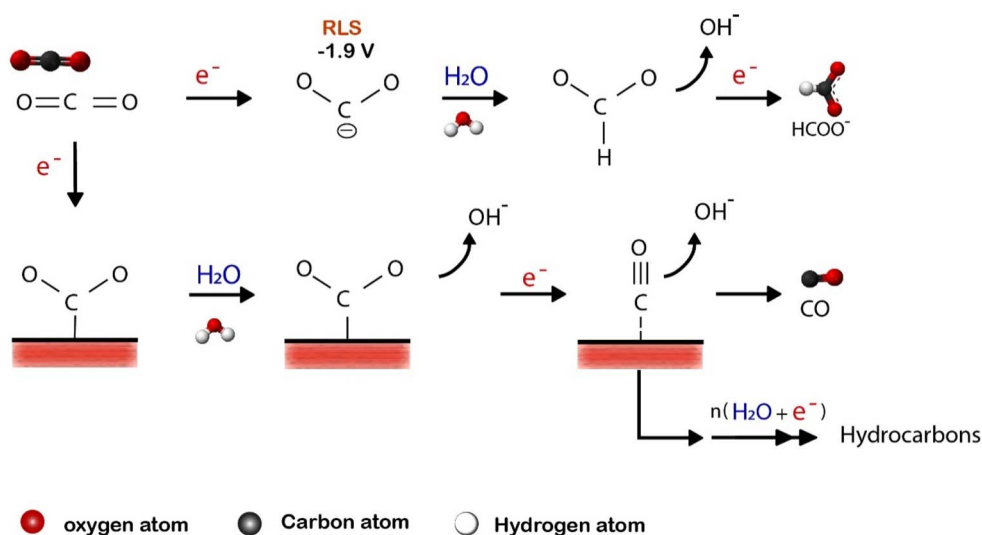| Product	Reduction potentials of CO_2	E° (V) *vs.* SHE (pH 7)
Carbon monoxide	$CO_2 + 2e^- + 2H^+ \rightarrow CO(g) + H_2O$	−0.53
Hydrogen	$2e^- + 2H^+ \rightarrow H_2(g)$	−0.42
Formic acid	$CO_2 + 2e^- + 2H^+ \rightarrow HCOOH(l) + H_2O$	−0.61
Formaldehyde	$CO_2 + 4e^- + 4H^+ \rightarrow CH_2O(l) + H_2O$	−0.50
Methanol	$CO_2 + 6e^- + 6H^+ \rightarrow CH_3OH(l) + H_2O$	−0.39
Methane	$CO_2 + 8e^- + 8H^+ \rightarrow CH_4(g) + H_2O$	−0.25
Ethylene	$CO_2 + 12e^- + 12H^+ \rightarrow C_2H_4(g) + 4H_2O$	−0.38
Ethane	$CO_2 + 14e^- + 14H^+ \rightarrow C_2H_6(g) + 4H_2O$	−0.28

Fig. 1 Most possible pathways for electrocatalytic CO_2RR on metal electrodes in aqueous solutions. Reproduced with permission from ref. 14. Copyright ©1994, Elsevier.

instantaneously within the potential range of -0.2 V to -0.6 V relative to SHE, resulting in a variety of CO_2 derivative products depending on the catalyst and electrolyte used.[14,44] There are two possible pathways in which CO_2^- can be reduced after it has been formed (Fig. 1). The first one is based on the protonation of CO_2^- oxygen atom, thus forming *COOH, which is further reduced to CO and desorbs from the electrode surface.[45,46] The second pathway is the protonation of CO_2^- carbon atoms to form HCOO* at high overpotential levels, which is further reduced to $HCOO^-$.[47]

The types and the number of target products are controlled by tuning the binding energy of the adsorbed intermediate such as (CO*, COOH*, CHO*, COH*).[48-50] For example, when the interaction between the surface of the electrocatalysts and the reduction intermediates is not strong enough, CO and $HCOO^-$ are the main reduction products. Because in the case of weak binding strength C–O bond does not dissociate. However, the electrocatalysts that bind CO* strongly produced a limited amount of CO and HCOOH because CO* intermediate will stick much longer on the surface of the catalyst, thus will be further reduced to other products.[51] Most CO_2 reduction electrocatalysts produce mainly CO and $HCOO^-$ products. However, only a few electrocatalysts, such as Cu, can further reduce CO to alcohols and hydrocarbons at low overpotentials.[18,52,53] The basic explanation for its potential to generate products apart from CO is that Cu binds *CO neither too weakly nor too strongly.[19]

3. Copper-based bimetallic materials

In literature, there is numerous method used to deposit a layer of metal onto another metal, ranging from physical deposition methods:[55] electron beam evaporation, pulsed layer deposition, sputtering to the chemical deposition methods:[56,57] chemical vapor deposition, atomic layer deposition; some of these methods are expensive due to the need of vacuum system and others lack safety. However, electrochemical methods are generally simple and low-cost.[58] The electrodeposition is one of the major electrochemical techniques used to produce inorganic electrodes with more complex compositions.[59] It provides the main advantage of monitoring and controlling the thickness of the samples by simply varying the deposition current/potential.[60] This technique can be applied to various types of materials including oxides, phosphates, chalcogenides, and metals (e.g., monometallic, bimetallic, ternary compounds). Due to its low cost and easy scalability, electrodeposition is particularly appealing for producing catalyst electrodes for use in solar fuel production.[59] In this technique, the cations are reduced in the cathode, and the reactive metal anodes are dissolved and re-deposited to load onto the surface of cathode.

Copper, which is the magical element for CO_2 electrocatalysis giving a variety of C2 to C3 chemicals, holds a unique interest in the CO_2 electrocatalysis community. This uniqueness of Cu may lie in its moderate binding energy for some key intermediates, such as adsorbed hydrogen *H and adsorbed *CO,[61] which favors the protonation of *CO into deeper reduction products. The Cu surfaces can be modulated, tuned and controlled on various supports which leads to different reactions tracks and pathways encompassing intermediates, *CO dimerization, C–C coupling, C1–C2 coupling etc. Some authors have highlighted that the coalescence, fragmentation and aggregation of copper nanoparticles might cause a stability issues in Cu based electrocatalysts and others suggested that many factors are affecting the CO_2RR efficiency of Cu catalysts.[54,62] It is well known that properties of bimetallic catalysts are significantly different from their monometallic counterparts because of the change in the electronic structures. Additionally, the bimetallic configuration provides new active sites, thus optimizing the binding strengths between intermediates and active sites.[63,64]
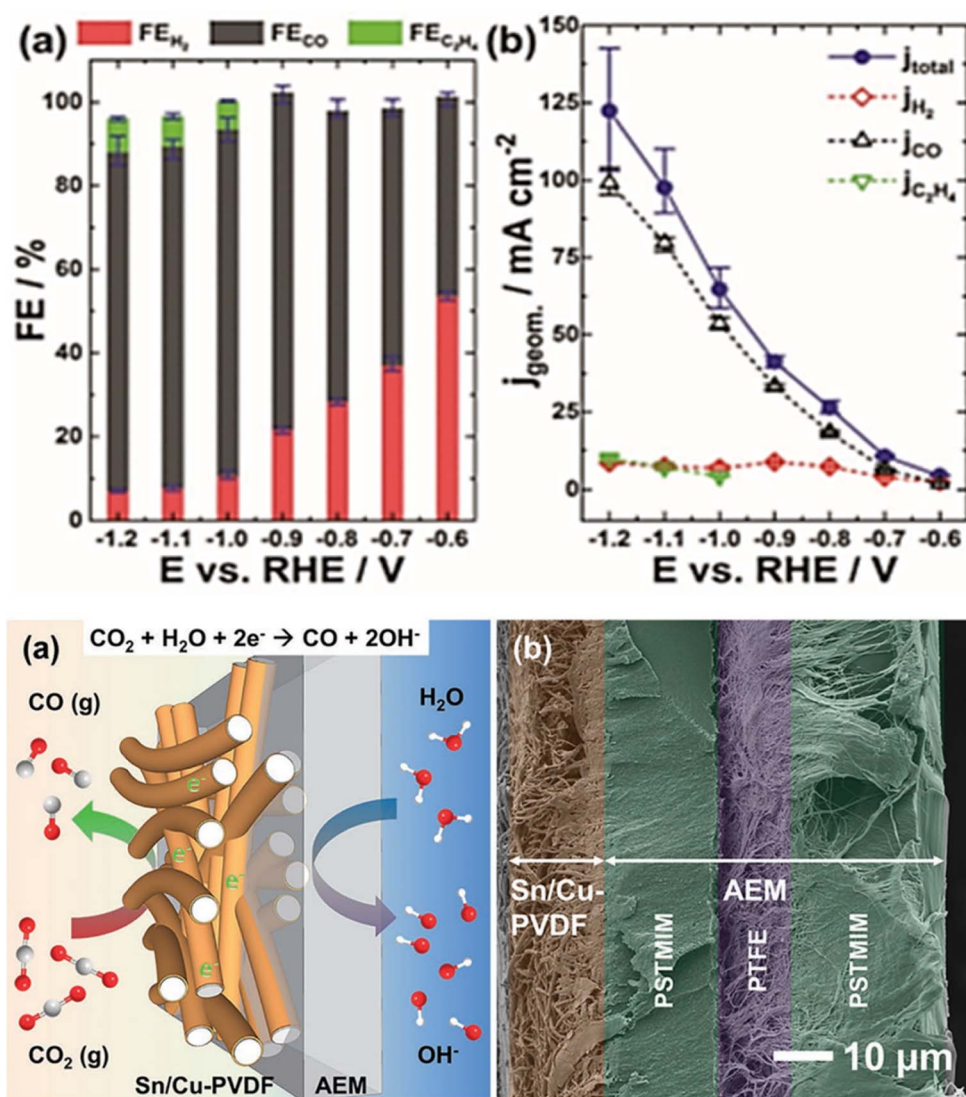
Fig. 2 (Up): (a) Faradaic efficiencies, (b) current densities for electrochemical CO_2 reduction at a Sn/Cu-PVDF GDE at (-0.6 to -1.2 V vs. RHE). (Bottom): (a) Scheme and (b) cross-sectional SEM image of a Sn/Cu-PVDF/AEM assembly used for electrocatalytic reduction of gaseous CO_2. Reproduced with permission.[66] Copyright ©2019, Wiley-VCH.

3.1 Cu–Sn bimetallic materials

Wang et al.[65] have reported the unexplored phase and structural engineering of Cu/Sn catalysts for enhancing CO_2 reduction reaction by simple thermal annealing of CuSn core–shell NPs in controlled conditions. $Cu-SnO_2$ catalysts were engineered with three distinct structures: the CuO/hollow SnO_2 heterostructure of CuSn NPs/C-A, the $Cu_{41}Sn_{11}@SnO_2$ core–shell structure of CuSn NPs/C–H and the Cu NPs/hollow SnO_2 Janus structure of CuSn NPs/C-AH. The electrocatalytic performance results showed that CO was the main product of the CO_2 reduction reaction under the potential of -0.7 V vs. RHE. The CuSn NPs/C-A catalyst achieved (70.1% FE_{CO}) and CuSn NPs/C-AH (45.1% FE_{CO}), which outperformed CuSn NPs/C–H (20.1% FE_{CO}), Cu NPs/C (13.5% FE_{CO}), and SnO_2 NSL/C 8.4% FE_{CO}). Furthermore, at the same potential (-0.7 V vs. RHE) the CuSn NPs/C-A exhibited the highest current density of CO approximately (1.66

mA cm^{-2}), which surpassed the CuSn NPs/C-AH (0.86 mA cm^{-2}) and Cu NPs/C (0.28 mA cm^{-2}) and was far better than the CuSn NPs/C–H (0.21 mA cm^{-2}) and SnO_2 NSL/C (0.05 mA cm^{-2}). It is clear that there was a selectivity transformation from CO to HCOOH when the electrolysis potential is changed from -0.7 V vs. RHE to -1.0 V vs. RHE. For all catalysts except Cu NPs/C, the main product of CO_2 reduction reaction was HCOOH. By contrast, CuSn NPs/C-A still exhibited the highest FE_{HCOOH} of 71.5%. Moreover, at -1.0 V vs. RHE, CuSn NPs/C-A reached the maximum partial current density of HCOOH around (12.6 mA cm^{-2}), which was higher than the values of the CuSn NPs/C-AH (mA cm^{-2} Cu NPs/C–H (10.5 mA cm^{-2}), Cu NPs/C, and SnO_2 NSL/C. In addition, the investigation of the stability using chronoamperometry at -0.7 V vs. RHE indicated that CuSn NPs/C-A, CuSn NPs/C-AH, CuSn NPs/C–H catalyst exhibited stable current densities in the span of 10 h. Ju et al.[66] demonstrated the importance of using CO_2 gaseous as a feedstock to enhance CO_2
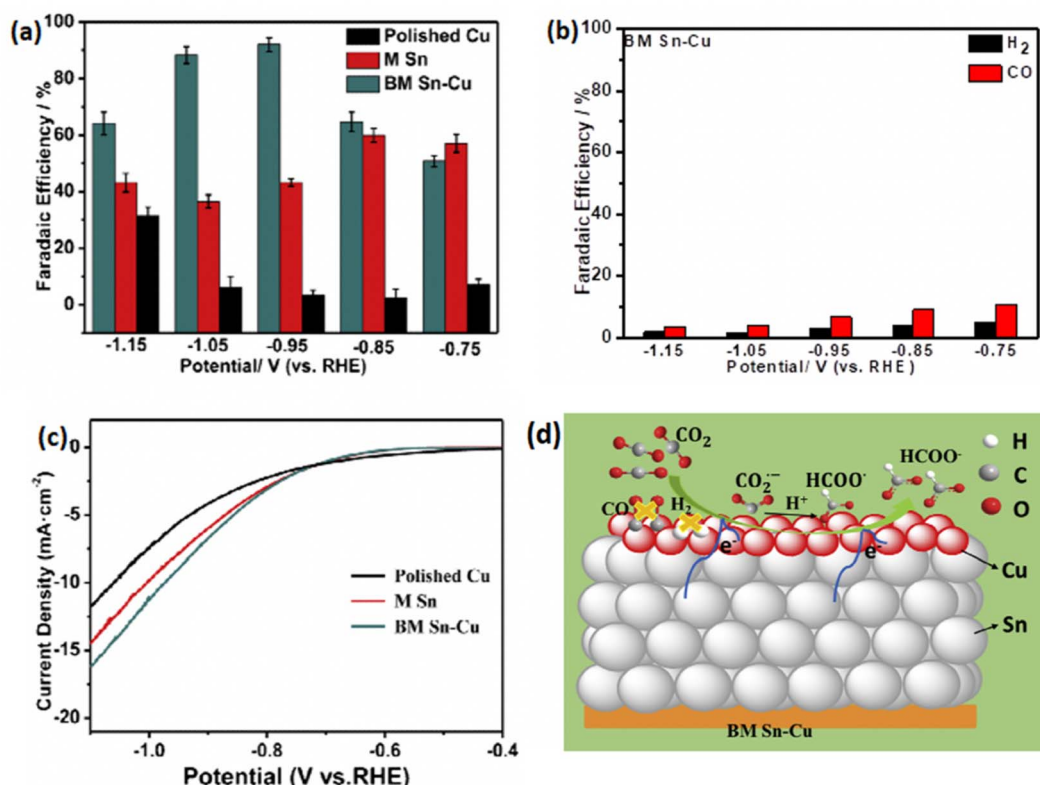
Fig. 3 (a) Faradaic efficiencies for $HCOO^-$ at potential range from -0.75 V to -1.15 V *vs.* RHE. (b) CO and H_2 faradaic efficiencies on the polished Cu, M Sn, BM Sn−Cu at potential range from -0.75 V to -1.15 V *vs.* RHE in saturated 0.1 M $KHCO_3$. (c) The partial current density of $HCOO^-$ on the polished Cu, M Sn, BM Sn−Cu, M Sn, BM Sn−Cu. (d) Proposed reaction mechanism for CO_2 electrochemical reduction to $HCOO^-$ of BM Sn−Cu electrode. Reproduced with permission.[67] Copyright ©2019, Elsevier.

mass transport and achieve high CO partial current density. In this regard, the authors employed Sn/Cu-nanofiber electrodes as freestanding gas diffusing electrodes GDEs. They fabricated electrospun polyvinylidene fluoride (PVDF) nanofibers with uniform Cu coating and then used electrochemical underpotential deposition (UPD) to decorate the surface of Cu with Sn. The faradaic efficiencies for CO (Fig. 2) were above 80% at potential ≤ -0.9 V and the partial current densities for CO exhibited 104 mA cm^{-2} at -1.2 V. However, at potentials ≤ -1.0 V a sparse amount of C_2H_4 less than 8.2% has been detected with current densities lower than 10 mA cm^{-2} (Fig. 2).

Furthermore, the Sn/Cu-PVDF GDE maintained long-term stability of 135 h at -1.0 V with the average CO FE (84.9%), while the average FEs for H_2 and C_2H_4 were 10.6% and 4.4%, respectively. In addition, it has been shown that the relatively high permeability of Sn/Cu nanofiber GDEs was essential for ensuring high CO_2 to CO conversion rates and inhibiting the hydrogen evolution reaction. Jiang *et al.*[67] provided a method for producing a high-performance bimetallic catalyst using an electronically regulated Cu in a heterogeneous bimetallic catalyst of Sn nanoparticles. The performance of the BM Sn−Cu catalyst was investigated under a wide potential range (from -0.75 V to -1.15 V *vs.* RHE). The BM Sn−Cu catalyst generated $HCOO^-$ as the primary product during CO_2 electrochemical reduction. As shown in (Fig. 3a) the BM Sn−Cu electrode

demonstrated the higher faradaic efficiency toward $HCOO^-$ about 92% at -0.95 V *vs.* RHE, while the total faradaic efficiency of CO and H_2 on the BM Sn−Cu electrode was less than 10% (Fig. 3b). The authors suggested that Sn plays a key in the enhanced catalytic performance of BM Sn−Cu catalyst toward $HCOO^-$. The electrocatalytic activity of Cu polished, BM Sn−Cu, and M Sn electrodes was examined under potentiostatic conditions in potential ranges from 0 to -1.2 V *vs.* RHE. The current density measurements (Fig. 3c) showed that among all electrodes, BM Sn−Cu electrode exhibited a higher $HCOO^-$ partial current density of 10.8 mA cm^{-2} at -0.95 V *vs.* RHE. This finding confirms that the embedded structure of BM Sn−Cu electrode can provide more active sites for CO_2 reduction. The DFT calculations were performed to understand the electronic structure of BM Sn−Cu catalyst for CO_2 electrochemical reduction. It was found that regulating the electronic structure of the catalyst promotes the formation of the HCOO* intermediate. Fig. 3d illustrates the proposed mechanism reaction for CO_2 electrochemical reduction to $HCOO^-$ on the BM Sn−Cu electrode.

Ye *et al.*[68] developed a new approach for designing the Cu−Sn alloy catalyst toward the electroreduction of CO_2 to $HCOO^-$ through a modified electrodeposition method. For the electrocatalytic performances, the Cu−Sn catalyst was evaluated under a wide potential range (from -0.7 V to -1.2 V *vs.* RHE). The Cu−
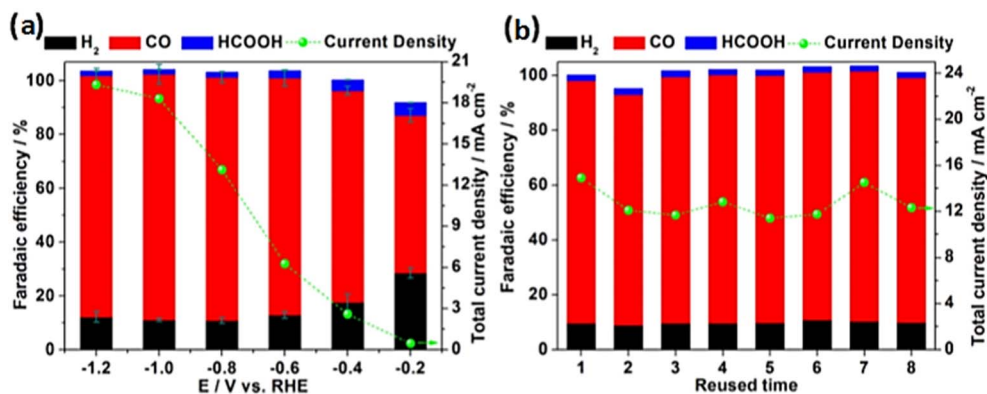
Fig. 4 (a) Effect of applied potential on product distribution and current density of c/s Cu Sn NW@foam for CO_2RR. (b) Stability of c/s Cu Sn NW@foam catalyst for CO_2RR by re-repeated use. Reproduced with permission.[70] Copyright ©2018, Wiley-VCH.

Sn catalyst produced $HCOO^-$ as the main product during CO_2 electrochemical reduction. The catalyst reduced the faradaic efficiency for H_2 evolution from (>90% at −0.75 V *vs.* RHE) to (less than 10% at −1.14 V *vs.* RHE) and improved the $HCOO^-$ faradaic efficiency reaching 82.3% at −1.14 V *vs.* RHE. In contrast, Sn on CFC catalyst exhibited $HCOO^-$ faradaic efficiency of greater than 55% at −1.14 V *vs.* RHE while few amounts of H_2 and CO were also obtained. The authors attributed the improved performance of Sn–Cu alloy catalyst towards $HCOO^-$ production to the stepped (211) surface of the Cu–Sn alloy. The $HCOO^-$ mass activity of Cu–Sn alloy catalyst increased along with increasing the applied potential reaching the maximum (1490.6 mA mg^{-1}) at −1.14 V *vs.* RHE. However, the $HCOO^-$ mass activity of the Cu–Sn catalyst decreased with the increase of the deposition time. The result showed that the highest mass activity was achieved at a deposition time of 0.01 s. Moreover, the authors investigated the correlation between CO_2RR performance and Sn deposition time. To this end, the results demonstrated that the faradaic efficiency of $HCOO^-$ remained stable at higher than 82% under various electrode-position times. Dong *et al.*[69] demonstrated the effect of the local corrosion phenomenon of Cu–Sn catalysts on the catalytic selectivity of CO_2 reduction *via* the pattering of the Sn layer on Cu foil. They found that the thickness of Sn patterns has a significant impact on the surface composition of Cu and Sn. In the Cu–Sn catalyst preparation, the Cu foil was electrochemically polished in the H_3PO_4 solution for 180 s by applying an anodic potential of 2.5 V *versus* the IrO_x counter electrode. Then, the Cu foil was cleaned with deionized water and dried using N_2 blowing.

For the photolithography process, the photoresist was spin-coated for 40 s at 6000 rpm and softly baked for 60 s at 110 °C. The photoresist-coated sample was moved to a mask aligner, and then the samples were contacted with a patterned photo-mask. The prepared Cu–Sn catalyst was sealed with epoxy except for the active area of the electrode (0.283 cm^2). In order to investigate catalytic performances, the authors prepared four samples denoted as Cu foil, Cu/Sn 3 nm, Cu/p-Sn 3 nm, and Cu/p-Sn 20 nm and they evaluated them at different applied potentials from −0.6 V to −1.2 V *vs.* RHE. The Cu foil obtained

a faradaic efficiency of greater than 50% at all potentials and began to produce CH_4 at high potentials (−1.2 V_{RHE}). In contrast, constructing a thick Sn layer 3 nm on Cu foil suppressed the H_2 evolution (FE_{H_2} < 5.5%) and increased the selectivity towards HCOOH (FE_{HCOOH} > 80%) at high potentials (from −0.8 V_{RHE} to −1.2 V_{RHE}). The Cu/p-S 3 nm exhibited unique selectivity towards CO, the faradaic efficiency reached the highest value (FE_{CO} = 58.1%) at −1.0 V *vs.* RHE. At a potential of −1.2 V_{RHE} the FE_{CO} of Cu/p-Sn catalyst decreased and FE_{CH_4} increased. On the other hand, Cu/p-Sn (20 nm) showed an increased selectivity towards HCOOH about 61.6% at −1.2 V_{RHE}. Furthermore, the authors investigated the effect of the pattering of Sn (t_{Sn}) on the catalytic selectivity of bimetallic Cu–Sn catalyst. They measured the faradaic efficiencies of Cu/Sn and Cu/p-Sn for various t_{Sn} values. The Cu/Sn catalyst with a thin Sn layer (t_{Sn} = 1 nm) exhibited a high CO FE of 86.1% at −1.0 V_{RHE}. However, the Cu/Sn catalyst with (t_{Sn} > 2 nm) showed a high FE_{HCOOH} of greater than 80% at −1.0 V_{RHE}. In comparison to Cu/Sn, the Cu/p-Sn catalyst with thin Sn patterns (between 2 nm to 4 nm) exhibited a high FE_{CO} of greater than 51.2%. However, increasing Sn patterns (t_{Sn} > 5 nm) resulted in a decrease in CO FE (40%) and an increased in HCOOH FE to 59.7%. Hu *et al.*[70] synthesized Cu–Sn core–shell nanowire array catalysts based on 3-D macroporous nickel (Ni) foams through two-step deposition annealing and electroreduction treatment. The electrochemical characterizations for CO_2RR revealed that constructing a Sn shell on Cu nanowires reduced faradaic efficiencies for H_2 from 55.7% to 10.1% and HCOOH formation from 12.3% to 2% and improved CO faradaic efficiency reaching 90% instead of 32% at an applied potential of −0.8 V *vs.* RHE. The authors attributed the improved performance to the suppressed adsorption of H* and the ordered arrangement of Sn and Cu atoms. Moreover, the authors investigated the correlation between CO_2RR performance and Sn deposition time. The results showed that the efficiency of CO increased with increasing the deposition time reaching the maximum at 10 s and then decreased with time while HCOOH, H_2 efficiencies are on an opposite trend. Furthermore, the effect of applied potential of c/s Cu–Sn NW foam was also investigated, indicating that the production selectivity toward CO remained

stable between -0.6 to -1.2 V with a faradaic efficiency higher than 90% and, the total current density reached -13.2 and -19.3 mA cm^{-2} between -0.8 to -1.2 V vs. RHE. In terms of stability, the Cu–Sn core/shell nanowire array catalyst exhibited good stability. After 8 cycles of use, the catalyst achieved stable current densities of 2 h for each cycle (Fig. 4). According to the authors, good stability could be ascribed to the formation of Cu$_6$Sn$_5$ in the interface.

Sarfraz et al.[71] prepared a highly CO selective catalyst by the electrodeposition of Sn on the surface of oxide-derived copper (OD-Cu). To elucidate the catalytic performance the authors prepared three samples: Sn deposited on OD-Cu denoted as (Cu–Sn), OD-Cu, and Sn deposited on Sn. The CO$_2$RR electrocatalytic showed that Cu–Sn exhibited a CO faradaic efficiency of greater than 90% over a wide potential range (from -0.5 to

-0.8 V vs. RHE), while only trace of HCOOH and H$_2$ were detected. Moreover, the Cu–Sn catalyst maintained long-term stability at least 14 h. The CO faradaic efficiency of OD-Cu catalyst increased with increasing the potential and reached a maximum ($\approx 63\%$) at -0.6 V vs. RHE and then drop to 32% at -0.8 V vs. RHE. In comparison, HCOOH faradaic efficiency increased along with increasing overpotential, reaching 45% FE at -0.8 V vs. RHE. On the other hand, Sn deposited on Sn electrode showed completely H$_2$ production. In addition, the authors have elucidated the effect of Sn deposition amount on the pre-reduced OD-Cu. The optimal amount of Sn was obtained at 3.9 µmol cm^{-2}, achieving selectivity of 90% CO FE and 5% HCOOH FE at -0.6 V vs. RHE; however, the excess of Sn deposited on OD-Cu favored H$_2$ generation. In order to investigate the catalytic performance of core–shell Cu–SnO$_2$

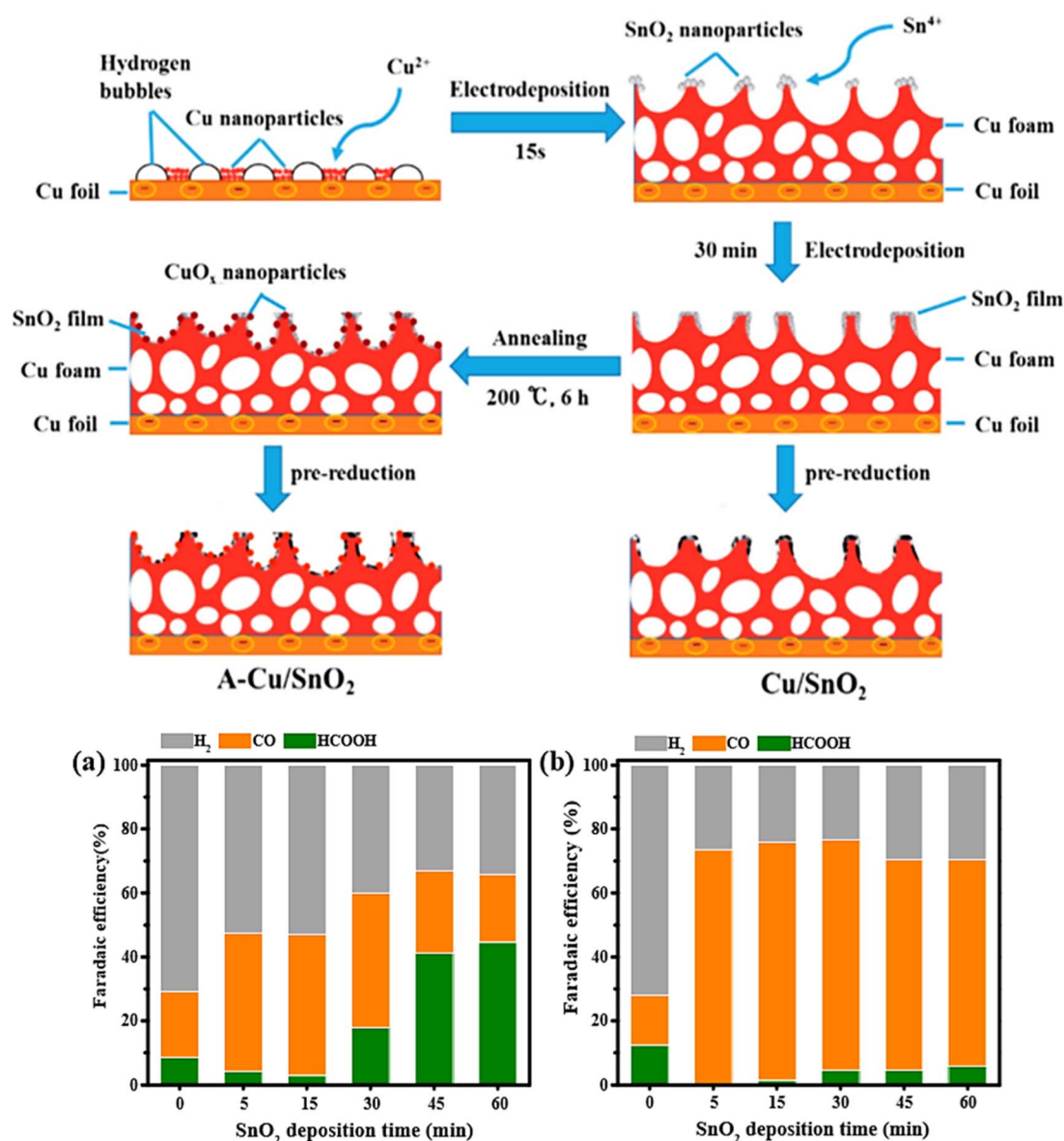Fig. 5 (Up) Schematic drawing of the fabrication of Cu/SnO$_2$ and A-Cu/SnO$_2$. (Bottom) Comparison of faradaic efficiencies of H$_2$, CO, and HCOOH for (a) Cu/SnO$_2$ and (b) A-Cu/SnO$_2$ electrodes with different deposition times at -1.0 V vs. RHE in CO$_2$-saturated 0.1 M KHCO$_3$.[73]

nanoparticles, Li *et al.*[72] synthesized two types of $CuSnO_2$ nanoparticles with the same core radius (7 nm) but different SnO_2 shell thicknesses (0.8 nm and 1.8 nm). They found that the thickness of Sn shell has a significant effect on product selectivity. The nanoparticles with thinner SnO_2 shell 0.8 nm (Fig. 5a) reached a maximum FE of 93% toward CO at −0.7 V *vs.* RHE with a current density of 4.6 mA cm^{-2}. The nanoparticles with thicker SnO_2 shell 1.8 nm (Fig. 5b) could produce 85% $HCOO^-$ at −0.9 V *vs.* RHE and less than 1% of CO formation. Based on density functional theory (DFT) calculations, the high selectivity of 0.8 nm SnO_2 shell toward CO was ascribed to the large compressive strain on the surface (10%), Cu doping on 0.8 nm SnO_2, and the less negative overpotential for CO (−1.87 V *vs.* RHE) compared to $HCOO^-$ (−2.21 V *vs.* RHE). To investigate the activity and the selectivity of Sn–Cu catalysis toward CO_2 reduction. Li *et al.*[73] engineered Cu/SnO_2 electrode by electro-depositing SnO_2 films on porous copper foam followed by electrochemical pre-reduction. The same procedure was used to fabricate the A-Cu/SnO_2 electrode, but with an additional annealing step. The Cu foil was mechanically polished with 200-grade sandpaper, electropolished in 85% of phosphoric acid, and washed with acetone and deionized water. Epoxy resin was used to encapsulate the back of Cu foil. The Cu foam was deposited on the pretreated Cu foil at a current density of −3 A cm^{-2} for 15 s in a plating bath containing (0.2 M $CuSO_4$, 1.5 M H_2SO_4). The Sn foil (2 cm × 2 cm) was electrodeposited on Cu foam electrode *via* electrodeposition method using a constant potential of −0.3 V while varying deposition time (5, 15, 30, 45, and 60 min) in the electrolyte consisting of (0.02 M $SnCl_4$, 0.1 M $NaNO_3$, 0.075 M HNO_3). The electrochemical pre-reduction was carried out in a CO_2- saturated 0.1 M KCO_3 at −0.5 V *vs.* RHE for 1 h. The resultant electrode was labeled as Cu/SnO_2 electrode. A-Cu/SnO_2 electrode was obtained by applying an additional annealing step (200 °C for 6 h in muffle furnace) between electrodepositing and pre-reduction processes (Fig. 5).

For the electrocatalytic performance, Cu/SnO_2 and A-Cu/SnO_2 were evaluated under a wide potential range (from −0.8 V to −1.2 V *vs.* RHE). The Cu/SnO_2 catalyst achieved 75% of H_2 FE and 25% of CO FE at −0.8 V *vs.* RHE. In contrast, A-Cu/SnO_2 exhibited a higher selectivity reaching nearly 60% FE at −0.8 V *vs.* RHE and a significant decrease of FE of H_2 approximately 40% at −0.8 V. This comparison indicated that A-Cu/SnO_2 has not only higher selectivity toward CO than Cu/SnO_2, but also higher CO_2 reduction activity. Furthermore, the authors investigated the effect of SnO_2 deposition time on Cu foam for both electrodes Cu/SnO_2 and A-$CuSnO_2$ at −1.0 V *vs.* RHE. In the case of Cu/SnO_2 electrodes, the efficiency of HCOOH increased with increasing the deposition time reaching the maximum at 60 min, while H_2 efficiency decreased along with increasing the deposition time. In contrast, CO FE achieved a higher level at 30 min and then decreased dramatically at 45 min of SnO_2 deposition time, and has since continued to decline. For A-Cu/SnO_2 with different deposition times of SnO_2, the production selectivity remained almost constant at greater than 70% FE for CO, and the least formation product was for HCOOH with FE (<5%), with a remarkable suppression of hydrogen evolution reaction. In terms of stability, A-Cu/SnO_2 catalyst with a deposited time of

15 min exhibited long-term stability of about 10 h. The selectivity for CO was maintained around 75% during the 10 h electrolysis, and the total current density was kept well at −8.5 mA cm^{-2}.

This class of bimetallic is very interesting as it can be tuned by different synthesis method to prepare active electrode for CO_2RR. However, one of the main drawbacks of these Cu–Sn materials is their shortcoming to further reduce CO_2 to multi-carbon hydrocarbons and other oxygenates value added chemicals. Accordingly, these materials do not offer a promising way to obtain a clean renewable fuel of high energy density and close the carbon loop cycle. The main products of Cu–Sn are carbon monoxide and formic acid or it can be tuned from one to another by varying the Cu/Sn composition.[74] This is barrier towards viable utilization of these materials for CO_2 valorization to C2 and oxygenates.

3.2 Cu–In bimetallic materials

Luo *et al.*[75] synthesized Cu–In catalyst by simply depositing In^{3+} on $Cu(OH)_2$ NWs followed with mild oxidation and *in situ* electroreduction treatments. The $Cu(OH)_2$ nanowires were synthesized *via* simple chemical oxidation. For this purpose, Cu foil (1 cm × 1 cm) was cleaned with water and sonicated in acetone for 5 min. Then, it was further etched in a solution containing 2 M of HNO_3 for 5 min to remove surface impurities. After immersing the Cu foil in a solution consisting of (2.5 M NaOH, 0.125 M $(NH_4)_2 S_2O_8$) for 10 min to grow $Cu(OH)_2$ NWs, the color of the solution changed from reddish to dark cyan, indicating the formation of $Cu(OH)_2$ NWs.[76] Tin (In) was deposited by dipping Cu foil into a solution containing $InCl_3$ for 30 s. The catalyst was obtained by *in situ* electroreduction before the CO_2 electroreduction experiments.

The electrocatalytic performance showed that the CO faradaic efficiency of CuNWs has increased gradually reaching the maximum (45%) at −0.6 V before dropping significantly to 16% at −1.0 V. HCOOH selectivity increased steadily along with decreasing the applied potential reaching the highest FE at −0.9 V and then decreased gradually at −1.0 V. While H_2 exhibited a high FE > 50% at a potential between (−0.4 to −0.5 V).

In contrast, the $CuIn_{20}$ catalyst produced CO as a main product throughout the entire examined potential range. Thus, CO FE of $CuIn_{20}$ reached almost 95% in the range of −0.6 to −0.8 V.

The current density measurements of Cu NWs and $CuIn_{20}$ under potentiostatic conditions showed that the CO partial current density of $CuIn_{20}$ was 5 times higher than that of Cu NWs catalyst. The stability test of $CuIn_{20}$ and Cu NWs was carried out at an applied potential of −0.6 V. Initially, Cu NWs catalyst exhibited 50% CO FE and dropped to 32% after 12 h of operation. Whereas, the $CuIn_{20}$ catalyst exhibited a stable current density of nearly 1.7 mA cm^{-2} and maintained an average (90%) of CO FE in the span of 60 h. According to the authors, the long-term stability of $CuIn_{20}$ catalyst could be ascribed to its low sensitivity to metal impurities.

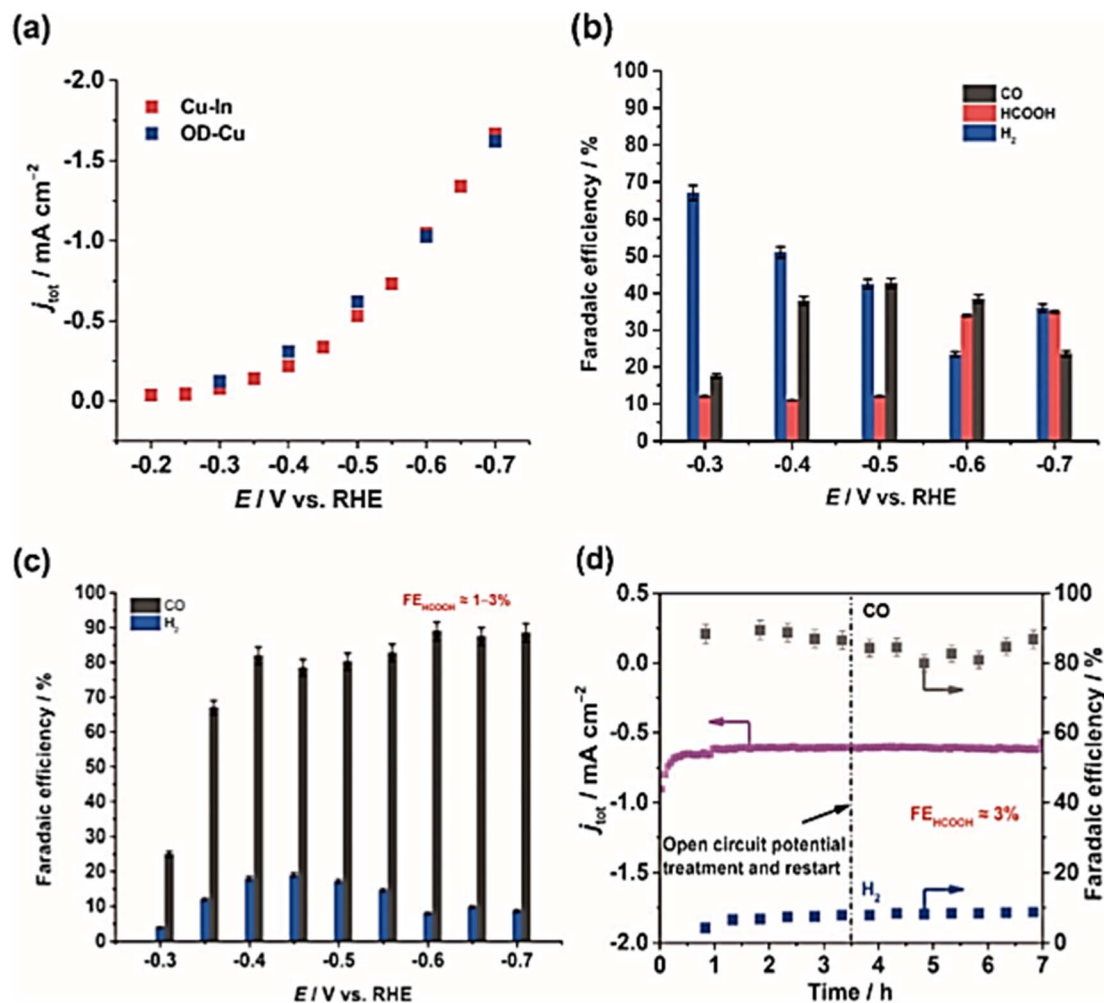The role of the In deposition amount on the CO_2RR was studied by immersing Cu NWs in various concentrations of

Fig. 6 (a) The current density of OD-Cu and Cu–In, (b) faradaic efficiencies of OD-Cu, (c) faradaic efficiencies of Cu–In, (d) test stability for the Cu–In catalyst at −0.6 V *vs.* RHE in 0.1 M $KHCO_3/CO_2$. Reproduced with permission.[77] Copyright ©2015, Wiley-VCH.

$InCl_3$ solution. The result showed that the current density and CO faradaic efficiency depended strongly on the In amount. It was found that CO FE increased with increasing In amount (0.52 μmol cm^{-2}) reaching a maximum of approximately 93% for $CuIn_{20}$ catalyst and then decreased for a higher amount of In.

Rasul *et al.*[77] developed a highly selective Cu–In electrocatalyst for the electrochemical reduction of CO_2 to CO. The Cu foil (1 cm × 3 cm) was cleaned in 1 M HCl for several seconds, rinsed with Milli-Q water, and dried at room temperature. The foil was further dried with Kimwipes to avoid partial oxidation of the electrode. OD-Cu electrode was obtained by thermally oxidizing Cu metal sheet at 500 °C for 2 h under static air in a muffle furnace. Afterward, Cu–In electrode was obtained through the *in situ* electrochemical reduction of the OD-Cu electrode in a solution consisting of (0.05 M $InSO_4$, 0.4 M citric acid) at a current density of −10 mA for 90 min.

The electrocatalytic performance of In–Cu and OD-Cu catalysts was investigated under a wide potential range potential from (−0.3 to −0.7 V *vs.* RHE). The results indicated that OD-Cu catalysts (Fig. 6b) produced mainly H_2 at −0.3 V. However, CO

and HCOOH selectivity increased along with increasing the applied potential and reached a maximum of 40% and 30%, respectively, at −0.6 V *vs.* RHE. In contrast, Cu–In electrode (Fig. 6a) exhibited a CO selectivity of 23% and a negligible H_2 level at −0.3 V *vs.* RHE. The conversion of CO_2 to CO increased with more negative polarization of the electrode, reaching a maximum faradaic efficiency of 95% at −0.7 V *vs.* RHE.

Cu–In and OD-Cu catalysts (Fig. 6c) exhibited similar values for total current density in the same electrochemical conditions. On the other hand, the stability of Cu–In catalyst (Fig. 6d) was evaluated at −0.6 V in 0.1 M $KHCO_3$, indicating good stability for 7 h with 85% CO FE.

3.3 Cu–Pd bimetallic materials

Palladium is as an intriguing catalyst owing to its low barrier toward H_2 adsorption and ease of formation of the metal hydride (PdHx).[78–81] It is regarded as a promising candidate for catalyzing CO_2 hydrogenation reactions and electrochemical CO_2 reduction reactions because it facilitates the hydrogenation and gives mainly CO in CO_2RR due to the hydride formation,
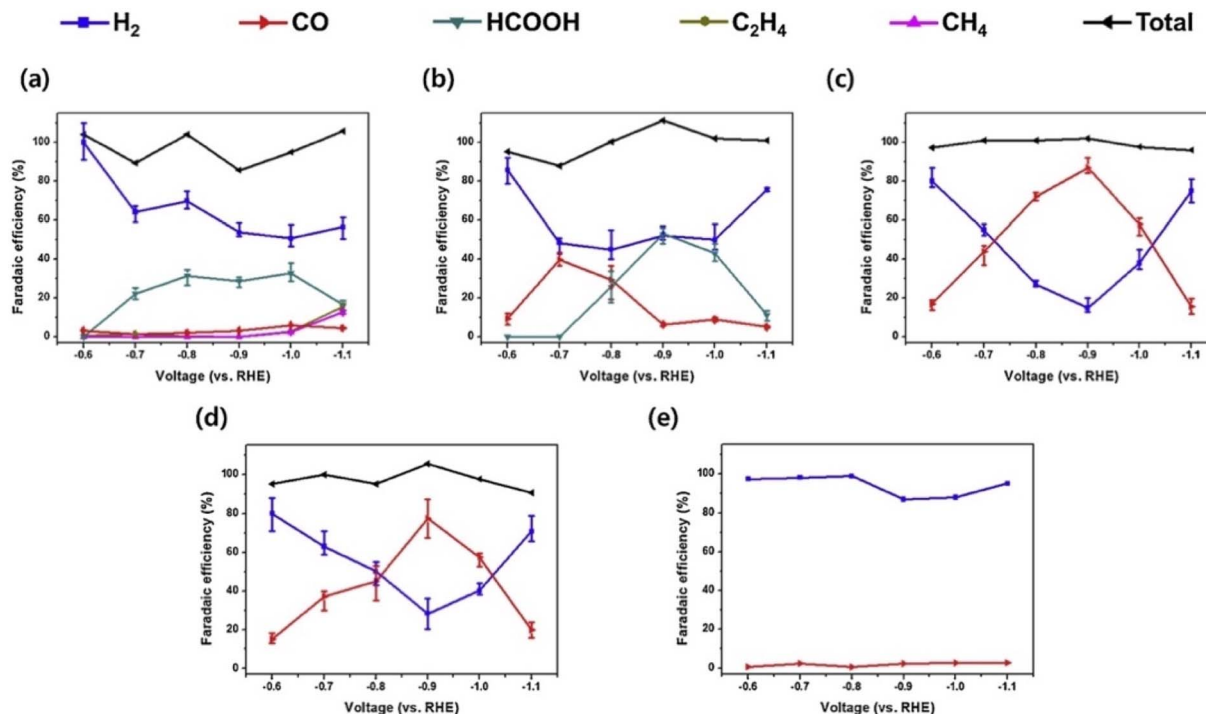
Fig. 7 Faradaic efficiencies of the Cu–Pd NP/C catalysts in 0.1 M KHCO$_3$ solution: (a) Cu NP/C, (b) Cu$_3$Pd NP/C, (c) CuPd NP/C, (d) CuPd$_3$ NP/C, and (e) Pd NP/C. Reproduced with permission.[84] Copyright ©2019, Elsevier.

which inhibits *CO binding and affects selectivity toward *COH/*CHO for further CO$_2$RR C$_2$ byproducts.[48,82]

For CO$_2$RR, Mun *et al.*,[83] have prepared monodisperse Cu–Pd nanoparticles (NPs) with various compositions *via* a colloidal method. Different products were obtained for when comparing with bulk copper catalyst. It was observed that alloying Cu to Pd suppresses hydrocarbon evolution and leads to CO production with a 1 : 1 Cu–Pd being the best electroactive catalyst giving 87% CO at −0.9 V *vs.* RHE (Fig. 7). The DFT results indicate that alloying Pd to Cu enhances the energy barrier of the CO protonation step, which is the potential-determining step for hydrocarbon production, resulting in a change in CO$_2$RR selectivity: Pd alloying causes H* to be more firmly adsorbed on CuPd(211) than on Cu(211), and the energy binding of adsorbed H* on Cu–Pd alloy is much lower energy than that of Cu(211), indicating that the HER is suppressed. The limiting potential of the favored CO* protonation step is higher on CuPd(211) (−1.03 V) than on Cu(211) (−0.60 V) and as reported elsewhere[50,82,84] the HCO* formation is much more favored than COH* formation on Cu(211), and on CuPd(211). This indicates the hydrocarbon suppression on Cu–Pd alloy.

Recently, Xie and coworkers[85] have prepared Cu–Pd heterostructures *via* dual potential electrochemical deposition which promotes CO$_2$ reduction and stabilizes CO* to preferable CH$_4$ formation. A small amount of HCOOH and C$_2$H$_4$ were observed. The aforementioned heterostructure exhibited a higher CO$_2$-to-CH$_4$ selectivity of 32% at high potentials of −1.2 and −1.25 V *vs.* RHE compared to the bare Cu and Pd metals. Using the DFT calculations, it was determined that adsorbed CO is the key

intermediate for CH$_4$ and C$_2$H$_4$ production which was in agreement with previous reports.[86,87]

A pyridine derivative abbreviated PYD was entrapped in Cu–Pd alloy to prepare and organically PYD@Cu–Pd composite for the CO$_2$RR to combine two active sites for alcohols electrosynthesis in a single catalyst. Cu nanoparticles (NPs), Pd NPs, Cu–Pd alloy, PYD@Cu and PYD@Pd composite were also prepared and tested as control experiments.[88] The PYD@Cu–Pd gives 26% and C$_2$H$_5$OH with 12% faradaic efficiencies at −0.04 and −0.64 V *vs.* RHE, respectively. Remarkably, the PYD@Pd and Cu–Pd yielded respectively 35% faradaic efficiency of CH$_3$OH at −0.04 V *vs.* RHE and 11% of C$_2$H$_5$OH at −0.64 V *vs.* RHE. This means that the PYD@Cu–Pd catalyses CO$_2$ to both CH$_3$OH and C$_2$H$_5$OH l using two active regions: Cu–Pd (For C$_2$H$_5$OH) and pyridine ring of PYD@Pd to PYD H* (CH$_3$OH).[89] Other control catalysts did not lead to alcohol formation. Longer stability screening for the PYD@Cu–Pd composite at constant cathodic potential of −0.04 and −0.64 V *vs.* RHE was reported for 14 h. The current density remained constant for both potential values, reaching 21 mA cm^{-2} and 5 mA cm^{-2} for CH$_3$OH and C$_2$H$_5$OH production, respectively, throughout the test. Moreover, the CH$_3$OH FE could maintain around 25% for 15 times repeated electrolysis and a small drop on the faradaic efficiency to C$_2$H$_5$OH was observed throughout the 15 cycles. This work shows the importance of the synergic effect of gathering organic catalyst and metal alloy in a very engineered fashion to put in work two alcohol sites for the CO$_2$RR.

Whereas, Wang and coworkers[90] have investigated the CuPd alloy with Pd rich surface supported on carbon for the CO$_2$RR to

HCOO$^-$ with 2 electron transfer. The prepared $Cu_{20}P8_{20}/C$ catalyst using adsorbate-induced surface segregation method shows a modest faradaic efficiency for the HCOO$^-$ electrosynthesis of 7.37%. When the same catalyst composition was prepared using by the NaH_2PO_2 reduction solution method instead of the H_2 thermal reduction process, the faradaic efficiency for HCOO$^-$ production increased to 60% at −0.75 V *vs.* Ag/AgCl. The authors have confirmed using *ex situ* XPS that the catalytic activity of the catalyst can be attributed to the lower bonding strength of H* (adsorbed hydrogen) on the $Cu_{20}Pd_{80}/C$ surface, which is promoted by the ligand effect between Cu and Pd as confirmed by the opposite band energy shift on Pd $3d_{5/2}$

and Cu $2p_{3/2}$ as well as the upshift of the d-band center for $Cu_{20}Pd_{80}/C$ NPs. Then, the lower bonding strength of hydride on the surface catalyst would reduce the activation energy barrier of the catalyst to transfer hydrogen from its surface to CO_2 and to form the HCOO* intermediate. Long-term chronoamperometry of 140 h have led to the CO catalyst poisoning and deactivation.

Carbon monoxide electroformation from CO_2RR was reported by Chen *et al.*,[91] using bimetallic Cu–Pd nanoalloys with different compositions and morphologies: spherical (noted as S) Cu–Pd nanoalloys with Cu/Pd molar ratio of 1/0.3 have the highest faradaic efficiency toward CO conversion (93%), while
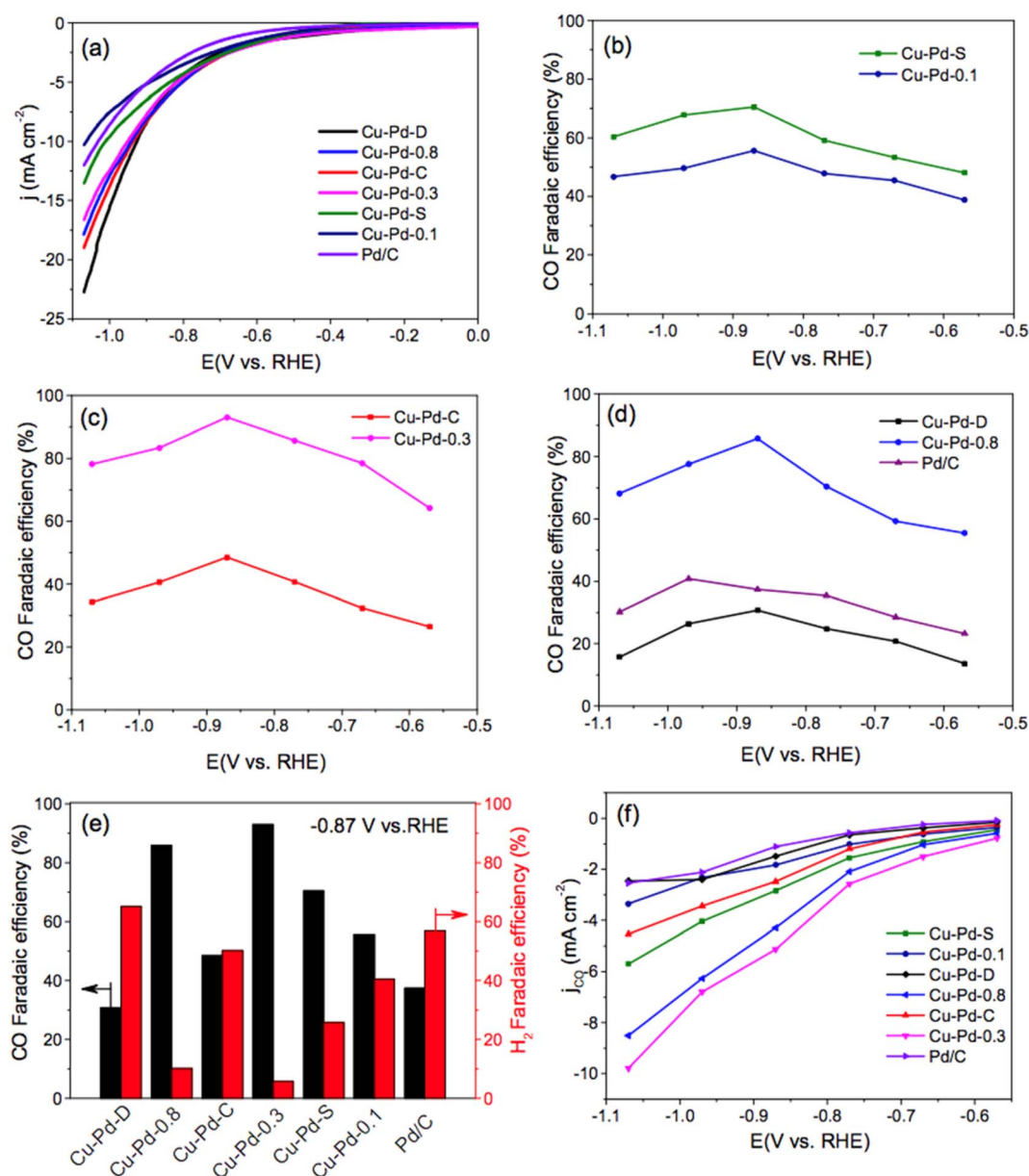

Fig. 8 LSV curves (a) of bimetallic Cu−Pd−S, Cu−Pd-0.1, Cu−Pd−C, Cu−Pd-0.3, Cu−Pd−D, Cu−Pd-0.8 nanoalloys, commercial Pd/C catalyst in CO_2 saturated 0.5 M $KHCO_3$ solution with a scan sweep of 10 mV s^{-1}, the CO faradaic efficiency at different applied potentials (b–d), the CO and H_2 faradaic efficiency at a fixed potential of −0.87 V (e), and CO partial current density of these nanoalloys (f). Reproduced with permission.[91] Copyright ©2018, American Chemical Society.

the dendritic Cu–Pd nanoalloys (noted as D) have the highest faradaic efficiency for H_2 (65.2%) via hydrogen evolution reaction at a polarized potential of -0.87 V vs. RHE (Fig. 8). While the concave nanocubes of Cu–Pd–C (noted as C) shows much lower CO FE. This work has shed light on the effect of morphologies on CO_2RR electroconversion, this will pave the way towards to catalysis by design and morphology dependent activity.

C_2 byproducts can be also formed through direct CO_2RR. For instance, Feng and coworkers[92] have prepared Cu–Pd catalysts using simple electrodeposition method on carbon paper. The electrochemical CO_2RR performance of the Cu–Pd/CP outperforms the bare Cu/CP and Pd/CP leading to higher current density suggesting favorable bonding and CO_2 activation. The faradaic efficiency of C_2H_4 reached 45.23%, at -1.2 V vs. RHE, whereas, Cu/CP recorded only 30% and no C_2H_4 on Pd/Pd catalyst. This reported C_2H_4 efficiency outperformed the state-of-the art metal catalysts reported elsewhere.[93–96] Ma et al.[97] investigated the effect of geometric arrangement on the Cu–Pd activity and selectivity. To this end, the authors synthesized different bimetallic Pd–Cu catalysts with disordered, ordered, and phase-separated atomic arrangements.

The electrocatalytic performance of CuPd bimetallic nanoparticles with distinct geometric arrangements exhibited different selectivity toward C_1 and C_2 products. For the ordered CuPd nanoparticles the faradaic efficiency toward C_1 products (mainly CO) achieved 80%, while C_2 products exhibited the lowest FE < 5%. However, the disordered CuPd nanoparticles reached a higher FE for CH_4 the ordered or phase-separated nanoparticles. In contrast, the phase-separated exhibited the highest FE 50% toward C_2 products (primarily C_2H_4). This could be due to the fact that the binding *CO in the phase-separated is less affected by the segregation of the two sites. Regarding the current density measurements, the phase-separated sample exhibited the highest total current density of 370 mA cm^{-2}, while the ordered sample achieved the lowest total current density. Furthermore, the authors investigated the correlation between the catalyst composition and its activity and selectivity. Therefore, they prepared two samples with different (Cu : Pd) ratios for the disordered structure: Cu_3Pd and $CuPd_3$. The electrochemical characterization showed that the CH_4 FEs for disordered CuPd were higher than that for both Cu_3Pd and $CuPd_3$. In addition, the FEs of C_2 products increased along with increasing Cu concentration.

Zhang et al.[98] reported an electrodeposition strategy for designing highly dispersed, ultrafine PdCu catalysts. PdCu catalyst exhibited a greater than two-fold enhancement in FE for CO_2 reduction to CH_4 as compared to the Cu catalyst. The maximum FE for CH_4 was 33% at -1.8 V (vs. Ag/AgNO$_3$). They indicated that the improvement was originated from a synergistic reaction between the Cu–CO and Pd–H sites during electrochemical CO_2 reduction. The onset of CO_2 reduction to CH_4 at the PdCu catalyst appeared at ~400 mV and ~200 mV more positive than at the Pd and Cu catalysts, respectively.

Chen et al.[99] prepared nanostructured Cu_2O-derived Cu catalyst and $PdCl_2$ for CO_2 to C_2H_6 conversion. The Cu_2O-derived Cu catalyst was prepared by the electrochemical deposition on Cu discs. When the addition of $PdCl_2$ was added into the catholyte during the CO_2 reduction at -1.0 V (vs. RHE), the C_2H_6 formation could be achieved with an FE of 30.1% at the same potential. According to their mechanistic studies, C_2H_4 was first produced from CO_2 reduction at the Cu sites. The hydrogenation occurred with the help of adsorbed $PdCl_x$ to produce C_2H_6. The efficient conversion of C_2H_4 to C_2H_6 required both copper and $PdCl_x$ sites. However, adding of other palladium-based particles to the electrolyte, such as Pd^0, PdO, or Pd–Al_2O_3, did not reach the same conversion efficiency.

Zhu et al.[100] employed thermal reduction treatment and in situ growth to prepare the CuPd catalyst. According to the electrocatalytic results, the FE of CuPd(100) catalyst achieved 50.3% at -1.4 V vs. RHE, which was higher than that of the Cu catalysts (23.6%) at the same potential. The CuPd(100) catalyst also had the highest electrochemically active surface area of 7.04×10^{-3} mF cm^{-2}. These results were consistent with the DFT prediction, implying that CuPd(100) could provide enough CO* for the C–C coupling by lowering the energy barrier of the CO_2* hydrogenation step.

Lai et al.[101] used a pulse program consisting of an open-circuit voltage (OCV) and a cathodic potential to investigate the effect of spontaneous reoxidation on the catalytic performance of Cu–Pd bimetallic catalysts. The results showed that the simultaneous presence of Cu and Pd was critical for achieving high CO FE for the bimetallic catalysts. Among all Cu–Pd catalysts, the Cu_5Pd_5 reached the maximum FE of 88% with the partial current density of -132 mA h g^{-1} at an applied cathodic potential of -0.7 V for 210 s and anodic potential at OCV for 450 s. The DFT calculation suggested that such efficient CO_2 conversion to CO resulted from the reduced *CO binding strength.

Li et al.[102] constructed a novel Cu–Pd catalyst Cu@PIL@Pd by impregnating PdCl2 into the Cu@PIL with Cl-as the anion. It was found that the Cu@PIL@Pd-2 catalyst exhibited the highest FE toward C_{2+} of 68.7% with a high partial current density of 178.3 mA cm^{-2} at a cathodic potential of -1.01 V vs. RHE. The catalyst also showed the highest CH_4 FE of 42.5% with a partial current density of 172.8 mA cm^{-2} at -1.24 V vs. RHE. The authors attributed the high selectivity of the Cu@PIL@Pd-2 catalyst toward C_{2+} products to the synergy effect between the adjacent Pd and Cu sites. The Cu was found to promote the CO generation on the Pd sites, while the abundant Cu–Pd interfaces promoted the *CO spillover from Pd sites to adjacent Cu sites, promoting the C–C coupling reaction.

Shen et al.[103] investigated CO electroreduction on a series of Cu–Pd catalysts prepared with different compositions: $Cu_{70}Pd_{30}$, $Cu_{49}Pd_{51}$, and $Cu_{23}Pd_{77}$. The results showed that the $Cu_{70}Pd_{30}$ catalyst produced acetate with a FE of >14% at -0.5 V vs. RHE and ethanol with a FE of 29% at -1.2 V vs. RHE. For the Pd-rich $Cu_{23}Pd_{77}$ catalyst, H_2 was the main product with a FE of >40% throughout the investigated potential range. In contrast, the $Cu_{49}Pd_{51}$ achieved a high selectivity toward acetate with a FE of >65% at -1.2 V vs. RHE. The acetate selectivity of $Cu_{49}Pd_{51}$ in the alkaline electrolyte was explained by the asymmetrical C–C coupling mechanism via *CO–*CHO coupling.

3.4 Cu–Zn bimetallic materials

Zinc (Zn) is environmentally friendly and less expensive as compared to other co-catalysts such as Ag, Pd, and Au.[104] Zn has attracted more attention due to its ability to reduce CO_2 to CO, HCOOH, and syngas at different overpotential.[105,106]

Because hydrogen evolution reaction occurs more slowly on Zn electrodes than on Cu electrodes,[107] forming bimetallic Cu–Zn catalyst is one approach to enhance the electrocatalytic activity of Cu electrode toward CO_2 reduction and promotes multicarbon products. Ren et al.[108] prepared a series of oxide-derived Cu_xZn catalysts to promote the reduction of CO_2 to C_2H_5OH. They revealed that introducing a co-catalyst improved the selectivity and the efficiency of CO_2 reduction.

Cu_xZn oxide films were prepared by dissolving 0.3 M $CuSO_4$ and 2.3 M lactic acid in ultrapure water. NaOH was added to the solution to adjust the pH to 12, 10.6, or 9. Then 10 mM of $ZnCl_2$ was added to the solution. The oxide films Cu_xZn were deposited onto Cu disks using a current density of -0.92 mA cm^{-2} for 10 min. During the deposition process, the electrolyte was kept at 960 °C and stirred at 300 rpm. The Cu_xZn catalysts exhibited
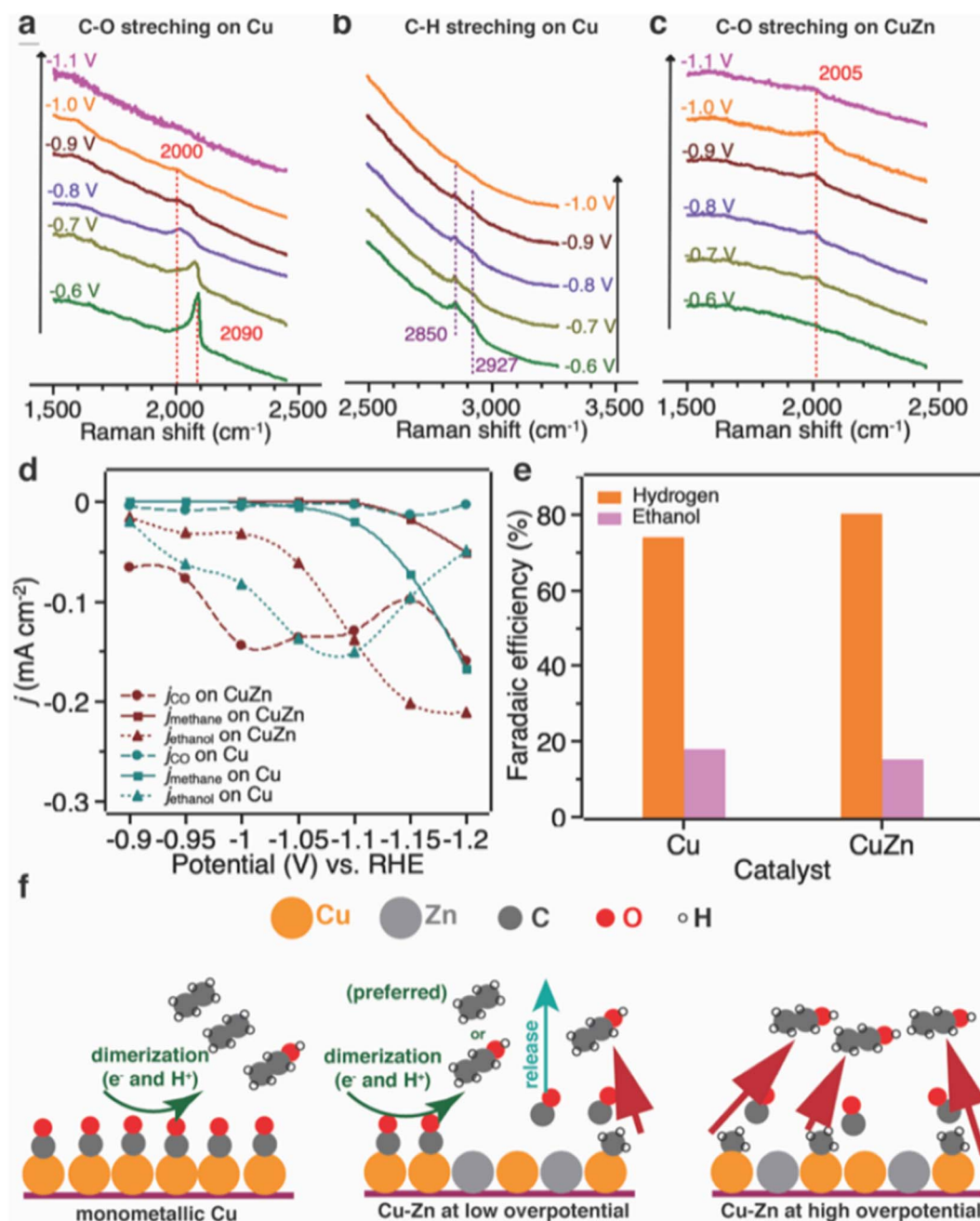

Fig. 9 *Operando* Raman spectrum of (a and b) Cu catalyst and (c) CuZn catalyst at different potentials in 0.1 M KHCO$_3$ under laser radiation at 785 nm; (d) partial current density (normalized against the electrochemical surface area) of C_2H_5OH, methane and carbon monoxide as a function of applied potential; (e) electrochemical reduction of acetaldehyde on Cu and CuZn catalyst; and (f) proposed mechanism of C_2H_5OH formation. Reproduced with permission.[111] Copyright ©2019, Wiley-VCH.

distinct selectivities toward C_2H_4 and C_2H_5OH formation. The faradaic efficiency of Cu_xZn catalysts toward C_2H_5OH increased along with increasing the amount of Zn, achieving the maximum FE of 29.1% on Cu_4Zn at -1.05 V vs. RHE. On the contrary, the faradaic efficiency toward C_2H_4 decreased along with increasing Zn amount, achieving the lowest FE of 4.1% on Cu_2Zn.

At -1.05 V vs. RHE, Cu_4Zn catalyst reached the highest partial current density of C_2H_5OH approximately -8.2 mA cm^{-2}, $Cu_{10}Zn$ catalyst achieved a partial current density of almost -4.0 mA cm^{-2} toward C_2H_5OH. Whereas Cu_2Zn exhibited the lowest partial current density of almost -2.3 mA cm^{-2} toward C_2H_5OH. Furthermore, Cu_4Zn catalyst maintained remarkable stability toward C_2H_5OH with a faradaic efficiency of 29.1% in the span of 5 h. However, the FE of C_2H_5OH decreased to 25% for 10 h electrolysis. The authors proposed a mechanism to elucidate the electroreduction of CO_2 to C_2H_5OH. In the first step, CO_2 is reduced to *CO at Cu or Zn sites and is then reduced to CHO or CH_x ($x = 1$–3) intermediates. Because of the weak adsorption of CO on Zn sites, desorbed CO could diffuse and overflow on the Cu sites. This CO could insert between Cu sites and *CH_2 to form *COH_2 which is further reduced to acetaldehyde and finally C_2H_5OH.

Keerthiga and Chetty[109] used a simple electrodeposition approach to design a hierarchically structured Zn electrocatalyst on Cu electrode. They prepared two samples Cu/Zn-A (in electrolytic bath containing 0.6 M of sodium zincate) and Cu/Zn-B (in electrolytic bath containing 6 M of sodium zincate). For the electrocatalytic performances, the prepared catalysts were evaluated under a wide potential range (from -0.7 V to -1.8 V vs. NHE). The Cu/Zn-B catalyst produced a maximum CH_4 formation of 52%, C_2H_6 formation of 24%, and H_2 formation of 8.7% at a potential of -1.6 V vs. NHE. Furthermore, the Cu/Zn-B catalyst exhibited a higher current density of 0.70 mA cm^{-2} for CH_4 at a potential of -1.6 V vs. NHE compared to the Cu (0.14 mA cm^{-2}) and Zn (0.01 mA cm^{-2}) electrodes. However, Cu/Zn-A catalyst produced mainly H_2, with only minor hydrocarbon formation. The results suggested that Zn deposition on Cu reduced hydrogen evolution and favored the addition of protons to form CH_4. The porous nature of hierarchically structured Zn could allow the diffusion of CO_2 through the Cu/Zn interface for the reduction while maintaining high catalytic activity due to the of the large electrode area of the hierarchical structure reducing the surface poisoning.

Su et al.[110] demonstrated the catalytic synergies of Cu and Zn to enhance the CO_2 electroreduction towards liquid C_2 products using hierarchically porous Cu/Zn catalysts.

The bimetallic catalysts were prepared based on an interfacial self-assembly method, in which the alloy composition of the catalysts can be adjusted by varying the ratios of metal precursors. The electrocatalytic performance results showed that hierarchically macroporous–mesoporous (HMMP) Cu_5Zn_8 demonstrated a high C_2H_5OH selectivity of 46.6% with C_2H_5OH current density of -2.3 mA cm^{-2} at -0.8 V vs. RHE. The Cu_5Zn_8 electrocatalyst maintained an excellent stability of 11 h towards CO_2 electroreduction. Grätzel and coworkers[111] prepared CuZn bimetallic catalyst by applying 100 atomic layer deposition

cycles of ZnO precursor on CuO nanowires. The obtained CuZn bimetallic catalysts exhibited 32% FE for C_2H_5OH production and C_2H_5OH current density of -10.5 mA cm^{-2} at -1.15 V vs. RHE. Based on their understanding, the authors proposed a mechanism of C_2H_5OH formation on Cu and CuZn catalysts (Fig. 9). On Cu catalyst, C_2H_4 and C_2H_5OH are produced through the dimerization of two adsorbed CO, resulting in the formation of C_2H_4. On CuZn catalyst, the CO produced on Zn sites tends to be released into the electrolyte due to the low binding energy between CO and Zn. At low overpotential, the formation of *CH_3 intermediate is minimal, and most of CO is released as CO gas. At higher overpotential, the *CH_3 intermediate is produced in large amounts and combines with the CO present near Cu sites to form C_2H_5OH.

Dongare et al.[112] engineered oxide derived CuO–ZnO_x bimetallic catalysts via a simple co-precipitation method followed by an air atmosphere calcination step. The loading percentage of Cu to Zn in the electrocatalysts was adjusted by varying the precursor concentrations from $x = 5$ to 20 wt%. The performance of the CuO–ZnO_x electrocatalysts was investigated under a wide potential range from -0.4 V to -1 V vs. RHE. The CuO–ZnO_x electrocatalysts demonstrated different FE for HCOOH, C_2H_5OH, CH_3OH, and n-propanol depending on the precursor concentrations. The CuO electrode showed low selectivity for C_2H_5OH about 7.10% of FE. In contrast, incorporating ZnO into CuO improved C_2H_5OH selectivity while suppressing the formation of HCOOH. Interestingly, CuO–ZnO_{10} electrode showed the highest faradaic efficiency of 22.27% for C_2H_5OH at -0.8 V vs. RHE. While, further increase in Zn concentration decreased the FE of C_2H_5OH to approximately 16.41% for CuO–ZnO_{20} electrode. Similar trend was found in the case of n-propanol and CH_3OH. The FE of n-propanol increased from 4.5% to 10.23% using CuO and CuO–ZnO_{10} respectively at -0.6 V vs. RHE, and the FE of CH_3OH increased from 7.44 to 15.02% on CuO and CuO–ZnO_{10} electrodes at -0.6 V vs. RHE. The authors claimed that the balanced CuO and ZnO percentage for maximum C–C coupling was responsible for the improved selectivity. The CuO–ZnO_{10} electrode gave a balanced CO supply, resulting in increased CO dimerization. The ZnO provided additional CO to increase the local CO concentration on the Cu surface and as a result, *CO surface coverage, resulting in a faster conversion of CO-to-C_2H_5OH products. Furthermore, increasing Zn concentration in the CuO–ZnO_x electrode beyond 10% results in as oversupply of CO, which lowered the *CO dimerization.

The stability and long-term durability of CuO–ZnO_{10} electrode was also investigated. During 12 hours of operation, the CuO–ZnO_{10} electrode maintained a total current density of -3.75 mA cm^{-2} with no change in the electrode morphology. The reproducibility experiments on CuO–ZnO_{10} electrode revealed that the selectivity of C_2H_5OH was maintained for first three cycles but decreased for subsequent cycles.

3.5 Cu–Ag bimetallic materials

Hoang et al.[113] aimed to enhance CO_2 selectivity towards C_2 products such as C_2H_4 and C_2H_5OH. For this purpose, Cu–Ag
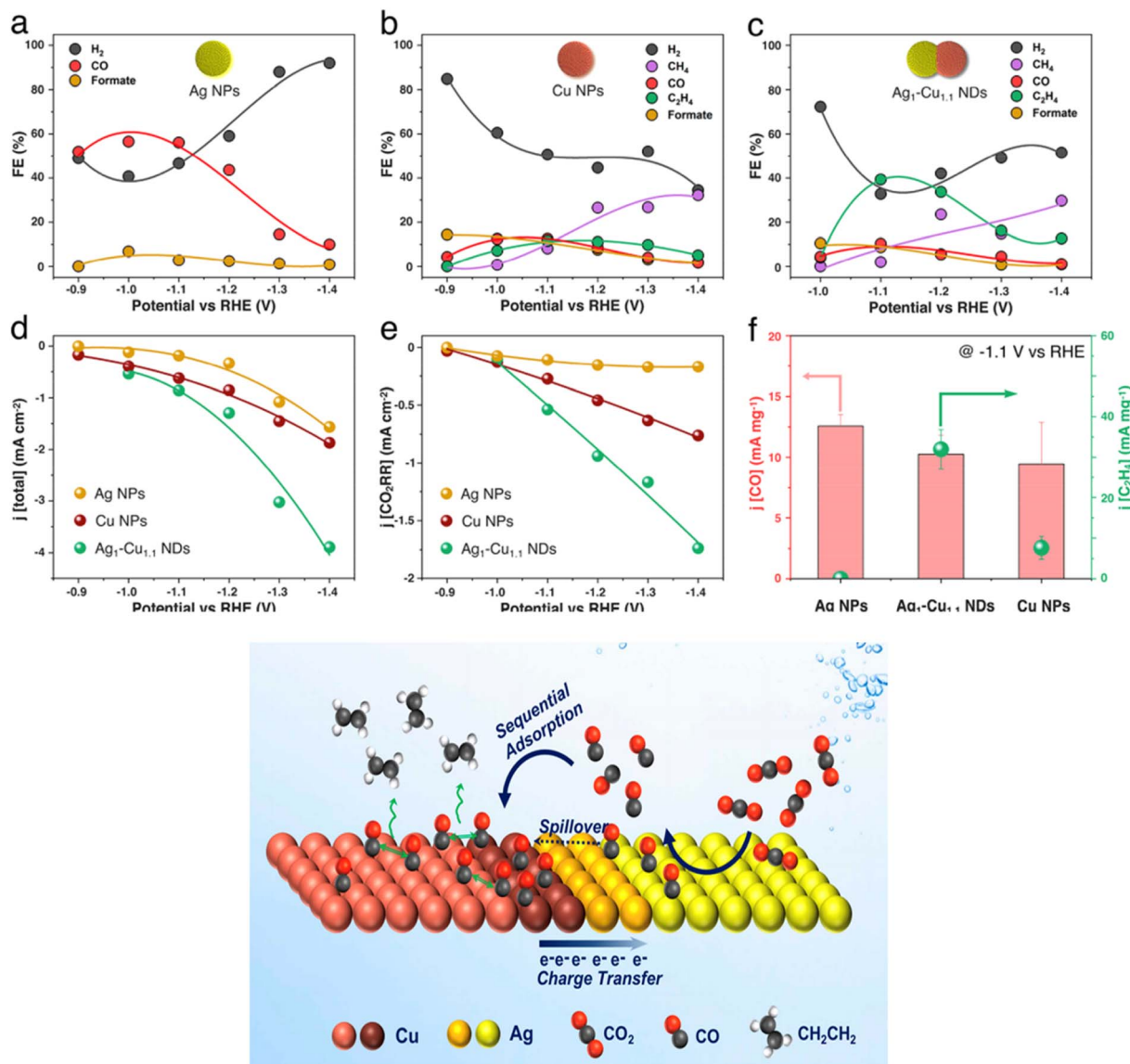
Fig. 10   (a–c) FEs for each gaseous product and for the main liquid product over (a) Ag NPs, (b) Cu NPs, and (c) $Ag_1–Cu_{1.1}$ NDs. (d and e) Total current density (d) and partial current density for the electroreduction of CO_2 (e) over Ag NPs, Cu NPs, and $Ag_1–Cu_{1.1}$ NDs. (f) CO and C_2H_4 mass activity of Ag NPs, Cu NPs and $Ag_1–Cu_{1.1}$ NDs at −1.1 V vs. RHE. Reproduced with permission.[114] Copyright ©2018, American Chemical Society.

catalysts were electrodeposited at a constant current density of 4 mA cm^{-2} in a plating bath containing 0.1 M $CuSO_4 \cdot 5H_2O$ + 3.5 diamino-1,2,4 triazole (DAT), with or without 1 mM Ag_2SO_4, at pH = 1.5 adjusted by using H_2SO_4. (1 cm × 2.5 cm) of carbon paper was activated by immersing it in concentrated HNO_3 for 60 min and used as a gas diffusion electrode before being electrodeposited with 2 C cm^{-2} of CuAg. The catalytic activity and selectivity of Cu and CuAg catalysts during CO_2 electro-reduction were evaluated in a flow electrolyzer. CO, C_2H_4, and C_2H_5OH were the major products using Cu-wire 0% Ag named (Cu-wire), CuAg-wire (6% Ag) electrodeposited with DAT named (CuAg-wire), and CuAg-wire (6% Ag) electrodeposited without DAT named (CuAg-poly).

The electrocatalytic results showed that the catalysts exhibited different activities and product selectivities in 1 M KOH electrolyte. The CuAg-poly catalyst exhibited the lowest faradaic efficiency nearly 30% toward C_2H_4 and 20% toward C_2H_5OH at −0.7 V vs. RHE. Furthermore, CuAg-poly catalyst exhibited a low current density approximately −20 mA cm^{-2} toward CO, C_2H_4, and C_2H_5OH. Cu-wire catalyst achieved high faradaic efficiency as well as high current density toward C_2 products. The faradaic efficiency for C_2H_4 increased along with increasing the potential reaching the maximum (40%) at low potential (−0.5 V vs. RHE), and C_2H_4 current density reached −100 mA cm^{-2} at −0.7 V vs. RHE. However, for the C_2H_5OH product, Cu-wire exhibited a faradaic efficiency of 20% at −0.5 V vs. RHE and a current density of −75 mA cm^{-2} at −0.7 V vs. RHE. In contrast, CuAg-wire catalyst achieved both high FE (60%) toward C_2H_4 and high C_2H_4 current density about- 180 mA cm^{-2} at −0.7 V vs. RHE. This high FE of C_2H_4 could be ascribed to the high pH solvent. Huang et al.[114] have prepared Ag–Cu nanodimers for CO_2-to-CO reduction, authors performed

a synthesis Ag–Cu with different compositions. The catalytic activity enabled by the addition of Ag to Cu in the form of segregated nanodomains within the same catalyst accounts for a 3.4-fold increase in faradaic efficiency for C_2H_4 and 2-fold increase in partial current density for CO_2 reduction when compared to the pure Cu counterpart. The FE of C_2H_4 electrosynthesis reached around 40% at −1.1 V $vs.$ RHE (Fig. 10).

The Cu–Ag alloy was also used by Wang $et~al.$[115] as an interfacial catalyst for the electrochemical reduction of CO_2 to C_2H_4. The faradaic efficiency for C_2H_4 formation reached over 42%, which is more than twice as high as that of pure Cu catalyst at −1.1 V $vs.$ RHE. The Cu–Ag catalyst remains stable and produce steady state C_2H_4 for 30 h electrolysis. The mechanism formation C_2H_4 was explained by the steps as follows: (i) Ag nanoparticles capture CO_2, (ii) CO_2 molecule accepts one proton and one electron to form *COOH intermediate on Ag nanoparticle surface, (iii) *COOH accepts one proton and one electron to form *CO intermediate on Ag nanoparticle surface. (iv) Transfer of CO intermediate from Ag nanoparticle to Cu side via the Ag/Cu interface and finally (v) C_2H_4 is formed by coupling two CO molecules.

Wang $et~al.$[116] synthesized Cu–Ag bimetallic nanowire arrays as catalysts in three steps. First, thermal oxidation was used in ambient air to grow CuO/Cu_2O nanowires on copper mesh. Then, in the presence of H_2, thermal reduction was carried out to obtain Cu nanowires. Finally, the Cu–Ag bimetallic nanowires were produced via galvanic replacement between Cu nanowires and the Ag^+ precursor. This catalyst leads to a reduction of CO_2 to a multitude of C_1 and C_2 byproducts with $HCOO^-$ being the highest in faradaic efficiency at −0.6, −0.7 and −0.8 V $vs.$ RHE. Interestingly, at −0.8 V CH_3OH, C_2H_5OH and propanol were observed with small faradaic efficiency (around 8%).

Meyer's group[117] have succeeded to reduce CO_2 to acetate using monodispersed, ultrasmall Ag and Cu bimetallic nanoparticles on electrochemically polymerized poly-Fe(vbpy)$_3$(PF$_6$)$_2$ films. The authors showed that the 8 electrons transfer to produce acetate can be obtained using a ratio variation of Ag/Cu. The maximum faradaic efficiency for acetate production reached 21.2% at −1.33 V $vs.$ RHE. The presence of Ag on the surface of the cluster pair Cu_2–Ag_3 plays a crucial role in maximizing acetate production.

Whereas, Jaramillo's group[118] have prepared CuAg thin films using nonequilibrium Cu/Ag alloying by physical vapor deposition technique. The prepared thin films prepared were tested for CO_2 electroreduction, the faradaic efficiencies of different 2 electrons byproducts including H_2, CO and HCOOH and further reduced (>2e$^-$) hydrocarbon, alcohol, and carbonyl CO_2RR products were analyzed. The films containing Cu-rich and Ag-rich phases with substantial nonequilibrium interphase miscibility demonstrated that Ag miscibility into Cu is an effective strategy to promote the electrocatalytic CO_2R selectivity and activity toward liquid carbonyl products. This was attributed to lower surface binding energies of oxygen-containing intermediate species. The catalytic activity of CuAg $versus$ Cu toward more reduced products was decreased, while the activity toward hydrocarbons and HER was significantly suppressed. The

decreasing activity and selectivity to hydrocarbons and suppressing hydrogen was explained to be due to the Ag doping which weakens the Cu binding energy of *H species.

3.6 Summary of the performance of Cu-based catalysts for CO_2RR

Catalyst	Conditions	Highlighted product with FE
CuSn core–shell NPs:[65]	0.1 M KHCO$_3$, -0.7 V $vs.$ RHE	
CuSn NPs/c-A		CO (70.1%)
CuSn NPs/c-AH		CO (45.1%)
CuSn NPs/c-H		CO (20.1%)
Sn/Cu-PVDF electrode[66]	0.1 M KHCO$_3$, −0.9 V $vs.$ RHE	CO (80%)
Cu–Sn core shell nanowire[70]	0.5 M KHCO$_3$, −0.8 V $vs.$ RHE	CO (90%)
Sn/OD-Cu[71]	0.1 M KHCO$_3$, −0.6 V $vs.$ RHE	CO (90%), HCOO$^-$ (5%)
Core–shell Cu–SnO$_2$ NPs[72]	0.5 M KHCO$_3$	
0.8 nm thick	−0.7 V $vs.$ REH	CO (93%)
1.8 nm thick	−0.9 V $vs.$ RHE	HCOO$^-$ (85%)
A-Cu/SnO$_2$ (ref. 73)	0.1 M KHCO$_3$, −1.0 V $vs.$ RHE	CO (70%)
CuIn$_{20}$ (ref. 75)	0.1 M KHCO$_3$, −0.6 V $vs.$ RHE	CO (95%)
Cu–In electrode[77]	0.1 M KHCO$_3$, −0.7 V $vs.$ RHE	CO (95%)
Cu$_{0.75}$In$_{0.25}$	0.5 M NaHCO$_3$, −0.7 V $vs.$ RHE	CO (81%)
Cu$_4$Zn[119]	0.1 M KHCO$_3$, −1.05 V $vs.$ RHE	C$_2$H$_5$OH (29.1%)
Cu$_5$Zn$_8$ (ref. 120)	0.05 M KHCO$_3$, −1.5 V $vs.$ RHE	CO (80%)
Cu$_{94}$Ag$_6$ (ref. 113)	1 M KOH, −0.7 V $vs.$ RHE	C$_2$H$_4$ (60%), C$_2$H$_5$OH$_5$ (25%)
Cu$_{16}$Ag$_{84}$ (ref. 121)	0.5 M KHCO$_3$, −0.83 V $vs.$ RHE	CO (45%)
Ag$_{57}$Cu$_{43}$ (ref. 121)	0.5 M KHCO$_3$, −1.5 V $vs.$ RHE	CO (40%)
Ag–Cu core–shell (surface Ag : Cu = 1 : 0.6)	0.1 M KHCO$_3$, −1.06 V $vs.$ RHE	CO (5%), CH$_4$ (18%), C$_2$H$_4$ (25%)
Ag–Cu core–shell[122] (surface Ag : Cu = 1 : 7.63)	0.1 M KHCO$_3$, −1.06 V $vs.$ RHE	CO (82%)
Cu$_{38}$Cd$_{62}$ (ref. 123)	0.05 M KHCO$_3$, −1.12 V $vs.$ RHE	CO (43%), HCOO$^-$ (10%)
Ordered CuPd[97]	1 M KOH, −0.55 V $vs.$ RHE	CO (80%)
Phase separated CuPd[97]	1 M KOH, −0.75 V $vs.$ RHE	CO (17%), C$_2$H$_4$ (48%), C$_2$H$_5$OH (15%)
Disordered CuPd[97]	1 M KOH, −0.60 V $vs.$ RHE	CO (60%), CH$_4$ (1%), C$_2$H$_4$ (4%), C$_2$H$_5$OH (2%)
Pd$_{85}$Cu$_{15}$ (ref. 124)	0.1 M KHCO$_3$, −0.89 V $vs.$ RHE	CO (86%)
o-AuCu[125]	0.1 M KHCO$_3$, −0.77 V $vs.$ RHE	CO (80%)
Cu@Au[126]	0.5 M KHCO$_3$, −0.65 V $vs.$ RHE	CO (30%)

4. Challenges and prospects

Over the next few decades, fossil fuels may remain the main energy source. Mitigating the impact of waste CO_2 emissions is still a key issue in modern society. Electrocatalytic CO_2 reduction provides an intriguing method for reducing CO_2, by which CO_2 as a feedstock can be converted into fuel or value-added chemicals. Copper is a magic element that can give various CO_2RR byproducts. Controlling, tuning and modulating Cu surfaces and Cu-based bimetallic materials is necessary to achieve stable multi-carbon (*i.e.* targeted product) production. Regardless of structural control, fundamental understanding of electrolyte engineering, cell design, pressure, temperature should be also elucidated to give the working state of Cu electrodes. In this review, we have discussed the mechanism of CO_2 electrochemical reduction on various copper-based catalytic materials and how certain factors determine the product distribution and its selectivity including synthesis method, modification, surface morphology and structure. Copper-based catalyst materials currently occupy an important position in electrolysis due to their exceptional properties. Efficient and robust copper-based materials have been successfully prepared through enhanced synthetic strategies. These efforts embody the most important areas to understand the basics of CO_2 reduction and contribute positively to the development of new bimetallic catalysts. Regardless of the important steps that have been made in this direction and the encouraging research labor and production, we still feel that these following prospects should be taken into account:

• Develop other or existing chemical synthesis and modification technique that requires a straightforward design of the active sites in the general catalysis by design procedure. Thusly, more exploration of the modification steps should be explored.

• Explore and investigate other metals as they can give a better energy efficiencies and selectivity, for instance Sultan and coworkers have developed Al_2CuO_4 nanosheets uniformly covered with CuO nanoparticles giving high FE for ethylene (82.4%) and remarkable stability in reaction condition to 100 h; this material achieved high current density of 421 mA cm^{-2} in a flow cell.[127]

• In depth-understanding of CO_2RR mechanisms is still a challenging task due to the evolution of the active site and the reconstruction of Cu materials under reaction conditions.

• Apply advanced *operando* techniques and theoretical calculation methods are highly recommended to probe the oxidation state, the CO_2 activation, and possible reaction intermediates of the electrochemical synthesized Cu-based catalysts. This will help to reorient and guide synthesis researchers to efficiently prepare a desired active site for a given CO_2RR byproduct as well as understanding the reaction mechanism and provide further guidance for the catalyst development.

• Tremendous efforts should be directed towards the design and construction of larger CO_2 electrolyzer pilots. It should be noted that the high currents of the electrolyzer as well as the overall energy efficiency are key requirements for further commercialization of this technology.

It is trustworthy to note that the catalytic activity and stability of the reported electrocatalysts are still far away from the industrialization that usually requires long-term stability of more than 1000 h at a high current density of over 200 mA cm^{-2}.

Author contributions

Otmane Zoubir: writing the draft, writing – review & editing, literature analysis. Lahoucine Atourki: writing – review & editing; project administration, supervision and validation. Hassan Ait Ahsaine: writing the draft, project administration; supervision and validation. Amal BaQais: writing – review & editing.

Conflicts of interest

The author declares that he has no known competing financial interests or personal relationships that could have appeared to influence the work reported in this paper.

Acknowledgements

References

1 N. S. Spinner, J. A. Vega and W. E. Mustain, *Catal. Sci. Technol.*, 2012, **2**, 19–28.

2 W. Zhu, B. M. Tackett, J. G. Chen and F. Jiao, *Top. Curr. Chem.*, 2018, **376**, 41.

3 N. Uemoto, M. Furukawa, I. Tateishi, H. Katsumata and S. Kaneco, *ChemEngineering*, 2019, **3**, 15.

4 M. Mondal, S. Khanra, O. N. Tiwari, K. Gayen and G. N. Halder, *Environ. Prog. Sustainable Energy*, 2016, **35**, 1605–1615.

5 W. C. Chueh and S. M. Haile, *ChemSusChem*, 2009, **2**, 735–739.

6 M. Mikkelsen, M. Jørgensen and F. C. Krebs, *Energy Environ. Sci.*, 2010, **3**, 43–81.

7 S. Bai, H. Qiu, M. Song, G. He, F. Wang, Y. Liu and L. Guo, *eScience*, 2022, **2**, 428–437.

8 C. Liu, J. J. Gallagher, K. K. Sakimoto, E. M. Nichols, C. J. Chang, M. C. Chang and P. Yang, *Nano Lett.*, 2015, **15**, 3634–3639.

9 M. Schreier, J. Luo, P. Gao, T. Moehl, M. T. Mayer and M. Grätzel, *J. Am. Chem. Soc.*, 2016, **138**, 1938–1946.

10 X. Chang, T. Wang and J. Gong, *Energy Environ. Sci.*, 2016, **9**, 2177–2196.

11 Z. Cao, D. Kim, D. Hong, Y. Yu, J. Xu, S. Lin, X. Wen, E. M. Nichols, K. Jeong and J. A. Reimer, *J. Am. Chem. Soc.*, 2016, **138**, 8120–8125.

12 A. S. Hall, Y. Yoon, A. Wuttig and Y. Surendranath, *J. Am. Chem. Soc.*, 2015, **137**, 14834–14837.

13 M. Liu, Y. Pang, B. Zhang, P. De Luna, O. Voznyy, J. Xu, X. Zheng, C. T. Dinh, F. Fan and C. Cao, *Nature*, 2016, **537**, 382–386.

14 Q. Lu and F. Jiao, *Nano Energy*, 2016, **29**, 439–456.

15 Q. Lu, J. Rosen, Y. Zhou, G. S. Hutchings, Y. C. Kimmel, J. G. Chen and F. Jiao, *Nat. Commun.*, 2014, **5**, 1–6.

16 Z. Sun, T. Ma, H. Tao, Q. Fan and B. Han, *Chem*, 2017, **3**, 560–587.

17 M. Aresta, A. Dibenedetto and A. Angelini, *Chem. Rev.*, 2014, **114**, 1709–1742.

18 K. P. Kuhl, E. R. Cave, D. N. Abram and T. F. Jaramillo, *Energy Environ. Sci.*, 2012, **5**, 7050–7059.

19 A. Vasileff, C. Xu, Y. Jiao, Y. Zheng and S.-Z. Qiao, *Chem*, 2018, **4**, 1809–1831.

20 F. Chang, M. Xiao, R. Miao, Y. Liu, M. Ren, Z. Jia, D. Han, Y. Yuan, Z. Bai and L. Yang, *Electrochem. Energy Rev.*, 2022, **5**, 1–35.

21 D. Karapinar, C. E. Creissen, J. G. Rivera de la Cruz, M. W. Schreiber and M. Fontecave, *ACS Energy Lett.*, 2021, **6**, 694–706.

22 B. Yang, K. Liu, H. Li, C. Liu, J. Fu, H. Li, J. E. Huang, P. Ou, T. Alkayyali and C. Cai, *J. Am. Chem. Soc.*, 2022, **144**, 3039–3049.

23 Z. Han, D. Han, Z. Chen, J. Gao, G. Jiang, X. Wang, S. Lyu, Y. Guo, C. Geng and L. Yin, *Nat. Commun.*, 2022, **13**, 1–10.

24 Y. Jia, F. Li, K. Fan and L. Sun, *Adv. Powder Mater.*, 2022, **1**, 100012.

25 B. Zhang, Y. Jiang, M. Gao, T. Ma, W. Sun and H. Pan, *Nano Energy*, 2021, **80**, 105504.

26 Y. F. Nishimura, H.-J. Peng, S. Nitopi, M. Bajdich, L. Wang, C. G. Morales-Guio, F. Abild-Pedersen, T. F. Jaramillo and C. Hahn, *ACS Appl. Mater. Interfaces*, 2021, **13**, 52044–52054.

27 S. Gao, Y. Lin, X. Jiao, Y. Sun, Q. Luo, W. Zhang, D. Li, J. Yang and Y. Xie, *Nature*, 2016, **529**, 68–71.

28 X. Zheng, Y. Ji, J. Tang, J. Wang, B. Liu, H.-G. Steinrück, K. Lim, Y. Li, M. F. Toney and K. Chan, *Nat. Catal.*, 2019, **2**, 55–61.

29 H. A. Hansen, C. Shi, A. C. Lausche, A. A. Peterson and J. K. Nørskov, *Phys. Chem. Chem. Phys.*, 2016, **18**, 9194–9201.

30 D. Gao, I. T. McCrum, S. Deo, Y.-W. Choi, F. Scholten, W. Wan, J. G. Chen, M. J. Janik and B. Roldan Cuenya, *ACS Catal.*, 2018, **8**, 10012–10020.

31 E. L. Clark, C. Hahn, T. F. Jaramillo and A. T. Bell, *J. Am. Chem. Soc.*, 2017, **139**, 15848–15857.

32 Y. Li, F. Cui, M. B. Ross, D. Kim, Y. Sun and P. Yang, *Nano Lett.*, 2017, **17**, 1312–1317.

33 P. Grosse, D. Gao, F. Scholten, I. Sinev, H. Mistry and B. Roldan Cuenya, *Angew. Chem., Int. Ed.*, 2018, **57**, 6192–6197.

34 Z. Weng, Y. Wu, M. Wang, J. Jiang, K. Yang, S. Huo, X.-F. Wang, Q. Ma, G. W. Brudvig and V. S. Batista, *Nat. Commun.*, 2018, **9**, 1–9.

35 P. W. Atkins, J. De Paula and P. W. Atkins, *Physical Chemistry*, W.H. Freeman, New York, 2006.

36 J. Qiao, Y. Liu and J. Zhang, *Electrochemical reduction of carbon dioxide. Fundamentals and technologies*, CRC Press, 2016.

37 P. Basu, *Chapter 5-Gasification Theory and Modeling of Gasifiers' in Biomass Gasification and Pyrolysis*, Academic Press, Boston, 2010.

38 H. Hashiba, H. K. Sato, S. Yotsuhashi, K. Fujii, M. Sugiyama and Y. Nakano, *Sustainable Energy Fuels*, 2017, **1**, 1734–1739.

39 W. J. Durand, A. A. Peterson, F. Studt, F. Abild-Pedersen and J. K. Nørskov, *Surf. Sci.*, 2011, **605**, 1354–1359.

40 B. Khezri, A. C. Fisher and M. Pumera, *J. Mater. Chem. A*, 2017, **5**, 8230–8246.

41 A. M. Appel, J. E. Bercaw, A. B. Bocarsly, H. Dobbek, D. L. DuBois, M. Dupuis, J. G. Ferry, E. Fujita, R. Hille and P. J. Kenis, *Chem. Rev.*, 2013, **113**, 6621–6658.

42 L. Torrente-Murciano, D. Mattia, M. D. Jones and P. K. Plucinski, *J. CO2 Util.*, 2014, **6**, 34–39.

43 J. Wu, P. P. Sharma, B. H. Harris and X.-D. Zhou, *J. Power Sources*, 2014, **258**, 189–194.

44 M. A. Tekalgne, H. H. Do, A. Hasani, Q. Van Le, H. W. Jang, S. H. Ahn and S. Y. Kim, *Mater. Today Adv.*, 2020, **5**, 100038.

45 F. Calle-Vallejo and M. T. Koper, *Angew. Chem.*, 2013, **125**, 7423–7426.

46 J. H. Montoya, C. Shi, K. Chan and J. K. Nørskov, *J. Phys. Chem. Lett.*, 2015, **6**, 2032–2037.

47 J. Wu, Y. Huang, W. Ye and Y. Li, *Adv. Sci.*, 2017, **4**, 1700194.

48 X. Nie, W. Luo, M. J. Janik and A. Asthagiri, *J. Catal.*, 2014, **312**, 108–122.

49 Z. W. Ulissi, M. T. Tang, J. Xiao, X. Liu, D. A. Torelli, M. Karamad, K. Cummins, C. Hahn, N. S. Lewis and T. F. Jaramillo, *ACS Catal.*, 2017, **7**, 6600–6608.

50 H. A. Hansen, C. Shi, A. C. Lausche, A. A. Peterson and J. K. Nørskov, *Phys. Chem. Chem. Phys.*, 2016, **18**, 9194–9201.

51 M. K. Birhanu, M.-C. Tsai, A. W. Kahsay, C.-T. Chen, T. S. Zeleke, K. B. Ibrahim, C.-J. Huang, W.-N. Su and B.-J. Hwang, *Adv. Mater. Interfaces*, 2018, **5**, 1800919.

52 Y. Hori, K. Kikuchi and S. Suzuki, *Chem. Lett.*, 1985, **14**, 1695–1698.

53 Y. Hori, I. Takahashi, O. Koga and N. Hoshi, *J. Phys. Chem. B*, 2002, **106**, 15–17.

54 S. Nitopi, E. Bertheussen, S. B. Scott, X. Liu, A. K. Engstfeld, S. Horch, B. Seger, I. E. Stephens, K. Chan and C. Hahn, *Chem. Rev.*, 2019, **119**, 7610–7672.

55 *Handbook of Deposition Technologies for Films and Coatings*, ed. P. M. Martin, William Andrew Publishing, Boston, 3rd edn, 2010, pp. 1–31.

56 M. J. Hampden-Smith and T. T. Kodas, *Chem. Vap. Deposition*, 1995, **1**, 39–48.

57 J. E. Crowell, *J. Vac. Sci. Technol., A*, 2003, **21**, S88–S95.

58 I. M. Dharmadasa and J. Haigh, *J. Electrochem. Soc.*, 2006, **153**, G47.

59 G. V. Govindaraju, G. P. Wheeler, D. Lee and K.-S. Choi, *Chem. Mater.*, 2017, **29**, 355–370.

60 T. S. N. S. Narayanan, I.-S. Park and M.-H. Lee, in *Surface Modification of Magnesium and its Alloys for Biomedical Applications*, ed. T. S. N. S. Narayanan, I.-S. Park and M.-H. Lee, Woodhead Publishing, Oxford, 2015, pp. 29–87.

61 A. Bagger, W. Ju, A. S. Varela, P. Strasser and J. Rossmeisl, *ChemPhysChem*, 2017, **18**, 3266–3273.

62 H. Tabassum, X. Yang, R. Zou and G. Wu, *Chem. Catal.*, 2022, **2**, 1561–1593.

63 M. Sankar, N. Dimitratos, P. J. Miedziak, P. P. Wells, C. J. Kiely and G. J. Hutchings, *Chem. Soc. Rev.*, 2012, **41**, 8099–8139.

64 A. Wang, X. Y. Liu, C.-Y. Mou and T. Zhang, *J. Catal.*, 2013, **308**, 258–271.

65 P. Wang, M. Qiao, Q. Shao, Y. Pi, X. Zhu, Y. Li and X. Huang, *Nat. Commun.*, 2018, **9**, 4933.

66 W. Ju, F. Jiang, H. Ma, Z. Pan, Y. Zhao, F. Pagani, D. Rentsch, J. Wang and C. Battaglia, *Adv. Energy Mater.*, 2019, **9**, 1901514.

67 X. Jiang, X. Wang, Z. Liu, Q. Wang, X. Xiao, H. Pan, M. Li, J. Wang, Y. Shao, Z. Peng, Y. Shen and M. Wang, *Appl. Catal., B*, 2019, **259**, 118040.

68 K. Ye, A. Cao, J. Shao, G. Wang, R. Si, N. Ta, J. Xiao and G. Wang, *Sci. Bull.*, 2020, **65**, 711–719.

69 W. J. Dong, J. W. Lim, D. M. Hong, J. Y. Park, W. S. Cho, S. Baek, C. J. Yoo, W. Kim and J.-L. Lee, *ACS Appl. Energy Mater.*, 2020, **3**, 10568–10577.

70 H. Hu, Y. Wang, N. Du, Y. Sun, Y. Tang, Q. Hu, P. Wan, L. Dai, A. C. Fisher and X. J. Yang, *ChemElectroChem*, 2018, **5**, 3854–3858.

71 S. Sarfraz, A. T. Garcia-Esparza, A. Jedidi, L. Cavallo and K. Takanabe, *ACS Catal.*, 2016, **6**, 2842–2851.

72 Q. Li, J. Fu, W. Zhu, Z. Chen, B. Shen, L. Wu, Z. Xi, T. Wang, G. Lu and J. Zhu, *J. Am. Chem. Soc.*, 2017, **139**, 4290–4293.

73 Q. Li, M. Li, S. Zhang, X. Liu, X. Zhu, Q. Ge and H. Wang, *Catalysts*, 2019, **9**, 476.

74 M. Zhang, Z. Zhang, Z. Zhao, H. Huang, D. H. Anjum, D. Wang, J. He and K.-W. Huang, *ACS Catal.*, 2021, **11**, 11103–11108.

75 W. Luo, W. Xie, R. Mutschler, E. Oveisi, G. L. De Gregorio, R. Buonsanti and A. Züttel, *ACS Catal.*, 2018, **8**, 6571–6581.

76 W. Zhang, X. Wen, S. Yang, Y. Berta and Z. L. Wang, *Adv. Mater.*, 2003, **15**, 822–825.

77 S. Rasul, D. H. Anjum, A. Jedidi, Y. Minenkov, L. Cavallo and K. Takanabe, *Angew. Chem., Int. Ed.*, 2015, **54**, 2146–2150.

78 H. Conrad, G. Ertl and E. E. Latta, *Surf. Sci.*, 1974, **41**, 435–446.

79 L. L. Jewell and B. H. Davis, *Appl. Catal., A*, 2006, **310**, 1–15.

80 G. Kyriakou, M. B. Boucher, A. D. Jewell, E. A. Lewis, T. J. Lawton, A. E. Baber, H. L. Tierney, M. Flytzani-Stephanopoulos and E. C. H. Sykes, *Science*, 2012, **335**, 1209–1212.

81 S. Bai, Q. Shao, P. Wang, Q. Dai, X. Wang and X. Huang, *J. Am. Chem. Soc.*, 2017, **139**, 6827–6830.

82 A. A. Peterson and J. K. Nørskov, *J. Phys. Chem. Lett.*, 2012, **3**, 251–258.

83 Y. Mun, S. Lee, A. Cho, S. Kim, J. W. Han and J. Lee, *Appl. Catal., B*, 2019, **246**, 82–88.

84 T. Adit Maark and B. R. K. Nanda, *J. Phys. Chem. C*, 2016, **120**, 8781–8789.

85 J.-F. Xie, J.-J. Chen, Y.-X. Huang, X. Zhang, W.-K. Wang, G.-X. Huang and H.-Q. Yu, *Appl. Catal., B*, 2020, **270**, 118864.

86 J. Qiao, Y. Liu, F. Hong and J. Zhang, *Chem. Soc. Rev.*, 2014, **43**, 631–675.

87 A. A. Peterson, F. Abild-Pedersen, F. Studt, J. Rossmeisl and J. K. Nørskov, *Energy Environ. Sci.*, 2010, **3**, 1311–1315.

88 H.-P. Yang, S. Qin, S.-N. Yue, L. Liu, H. Wang and J.-X. Lu, *Catal. Sci. Technol.*, 2016, **6**, 6490–6494.

89 E. Barton Cole, P. S. Lakkaraju, D. M. Rampulla, A. J. Morris, E. Abelev and A. B. Bocarsly, *J. Am. Chem. Soc.*, 2010, **132**, 11539–11551.

90 W. J. Wang, S. Hwang, T. Kim, S. Ha and L. Scudiero, *Electrochim. Acta*, 2021, **387**, 138531.

91 D. Chen, Q. Yao, P. Cui, H. Liu, J. Xie and J. Yang, *ACS Appl. Energy Mater.*, 2018, **1**, 883–890.

92 R. Feng, Q. Zhu, M. Chu, S. Jia, J. Zhai, H. Wu, P. Wu and B. Han, *Green Chem.*, 2020, **22**, 7560–7565.

93 S. Jia, Q. Zhu, H. Wu, M. Chu, S. Han, R. Feng, J. Tu, J. Zhai and B. Han, *Chin. J. Catal.*, 2020, **41**, 1091–1098.

94 O. A. Baturina, Q. Lu, M. A. Padilla, L. Xin, W. Li, A. Serov, K. Artyushkova, P. Atanassov, F. Xu and A. Epshteyn, *ACS Catal.*, 2014, **4**, 3682–3695.

95 L. Hou, J. Han, C. Wang, Y. Zhang, Y. Wang, Z. Bai, Y. Gu, Y. Gao and X. Yan, *Inorg. Chem. Front.*, 2020, **7**, 2097–2106.

96 Y. Chen, Z. Fan, J. Wang, C. Ling, W. Niu, Z. Huang, G. Liu, B. Chen, Z. Lai and X. Liu, *J. Am. Chem. Soc.*, 2020, **142**, 12760–12766.

97 S. Ma, M. Sadakiyo, M. Heima, R. Luo, R. T. Haasch, J. I. Gold, M. Yamauchi and P. J. A. Kenis, *J. Am. Chem. Soc.*, 2017, **139**, 47–50.

98 S. Zhang, P. Kang, M. Bakir, A. M. Lapides, C. J. Dares and T. J. Meyer, *Proc. Natl. Acad. Sci. U. S. A.*, 2015, **112**, 15809–15814.

99 C. S. Chen, J. H. Wan and B. S. Yeo, *J. Phys. Chem. C*, 2015, **119**, 26875–26882.

100 L. Zhu, Y. Lin, K. Liu, E. Cortés, H. Li, J. Hu, A. Yamaguchi, X. Liu, M. Miyauchi and J. Fu, *Chin. J. Catal.*, 2021, **42**, 1500–1508.

101 Y.-A. Lai, Y.-C. Chu, C.-J. Chang, K.-H. Chen, Y.-C. Hsiao, C.-C. Chang, M.-Y. Liao and H. M. Chen, *Adv. Energy Sustain. Res.*, 2022, 2200075.

102 X.-Q. Li, G.-Y. Duan, X.-X. Yang, L.-J. Han and B.-H. Xu, *Fundam. Res.*, 2022, DOI: 10.1016/j.fmre.2021.12.009.

103 H. Shen, Y. Wang, T. Chakraborty, G. Zhou, C. Wang, X. Fu, Y. Wang, J. Zhang, C. Li and F. Xu, *ACS Catal.*, 2022, **12**, 5275–5283.

104 Z. Li, R. M. Yadav, L. Sun, T. Zhang, J. Zhang, P. M. Ajayan and J. Wu, *Appl. Catal., A*, 2020, **606**, 117829.

105 F. Quan, D. Zhong, H. Song, F. Jia and L. Zhang, *J. Mater. Chem. A*, 2015, **3**, 16409–16413.

106 B. Qin, Y. Li, H. Fu, H. Wang, S. Chen, Z. Liu and F. Peng, *ACS Appl. Mater. Interfaces*, 2018, **10**, 20530–20539.

107 J. Rosen, G. S. Hutchings, Q. Lu, R. V. Forest, A. Moore and F. Jiao, *ACS Catal.*, 2015, **5**, 4586–4591.

108 D. Ren, B. S.-H. Ang and B. S. Yeo, *ACS Catal.*, 2016, **6**, 8239–8247.

109 G. Keerthiga and R. Chetty, *J. Electrochem. Soc.*, 2017, **164**, H164.

110 X. Su, Y. Sun, L. Jin, L. Zhang, Y. Yang, P. Kerns, B. Liu, S. Li and J. He, *Appl. Catal., B*, 2020, **269**, 118800.

111 D. Ren, J. Gao, L. Pan, Z. Wang, J. Luo, S. M. Zakeeruddin, A. Hagfeldt and M. Grätzel, *Angew. Chem., Int. Ed.*, 2019, **58**, 15036–15040.

112 S. Dongare, N. Singh, H. Bhunia and P. K. Bajpai, *Electrochim. Acta*, 2021, **392**, 138988.

113 T. T. Hoang, S. Verma, S. Ma, T. T. Fister, J. Timoshenko, A. I. Frenkel, P. J. Kenis and A. A. Gewirth, *J. Am. Chem. Soc.*, 2018, **140**, 5791–5797.

114 J. Huang, M. Mensi, E. Oveisi, V. Mantella and R. Buonsanti, *J. Am. Chem. Soc.*, 2019, **141**, 2490–2499.

115 J. Wang, Z. Li, C. Dong, Y. Feng, J. Yang, H. Liu and X. Du, *ACS Appl. Mater. Interfaces*, 2019, **11**, 2763–2767.

116 Y. Wang, C. Niu and Y. Zhu, *Nanomaterials*, 2019, **9**, 173.

117 Y. Wang, D. Wang, C. J. Dares, S. L. Marquard, M. V. Sheridan and T. J. Meyer, *Proc. Natl. Acad. Sci. U. S. A.*, 2018, **115**, 278–283.

118 D. Higgins, A. T. Landers, Y. Ji, S. Nitopi, C. G. Morales-Guio, L. Wang, K. Chan, C. Hahn and T. F. Jaramillo, *ACS Energy Lett.*, 2018, **3**, 2947–2955.

119 D. Ren, J. Fong and B. S. Yeo, *Nat. Commun.*, 2018, **9**, 925.

120 A. Katoh, H. Uchida, M. Shibata and M. Watanabe, *J. Electrochem. Soc.*, 1994, **141**, 2054.

121 J. Choi, M. J. Kim, S. H. Ahn, I. Choi, J. H. Jang, Y. S. Ham, J. J. Kim and S.-K. Kim, *Chem. Eng. J.*, 2016, **299**, 37–44.

122 Z. Chang, S. Huo, W. Zhang, J. Fang and H. Wang, *J. Phys. Chem. C*, 2017, **121**, 11368–11379.

123 M. Watanabe, M. Shibata, A. Kato, M. Azuma and T. Sakata, *J. Electrochem. Soc.*, 1991, **138**, 3382.

124 Z. Yin, D. Gao, S. Yao, B. Zhao, F. Cai, L. Lin, P. Tang, P. Zhai, G. Wang and D. Ma, *Nano Energy*, 2016, **27**, 35–43.

125 D. Kim, C. Xie, N. Becknell, Y. Yu, M. Karamad, K. Chan, E. J. Crumlin, J. K. Nørskov and P. Yang, *J. Am. Chem. Soc.*, 2017, **139**, 8329–8336.

126 K. Chen, X. Zhang, T. Williams, L. Bourgeois and D. R. MacFarlane, *Electrochim. Acta*, 2017, **239**, 84–89.

127 S. Sultan, H. Lee, S. Park, M. M. Kim, A. Yoon, H. Choi, T.-H. Kong, Y.-J. Koe, H.-S. Oh and Z. Lee, *Energy Environ. Sci.*, 2022, **15**, 2397–2409.